

11-2020

**SYNTHESIS, CHARACTERIZATION, ELECTRONIC STRUCTURE OF
BiOCl/BiOBr/rGO TERNARY HETEROJUNCTION AND ITS
PHOTOCATALYTIC ACTIVITIES**

Salama Yousef Alismaail

Follow this and additional works at: https://scholarworks.uaeu.ac.ae/all_theses

 Part of the [Chemistry Commons](#)

United Arab Emirates University

College of Science

Department of Chemistry

SYNTHESIS, CHARACTERIZATION, ELECTRONIC STRUCTURE
OF BiOCl/BiOBr/rGO TERNARY HETEROJUNCTION AND ITS
PHOTOCATALYTIC ACTIVITIES

Salama Yousef Alismaail

This thesis is submitted in partial fulfilment of the requirements for the degree of
Master of Science in Chemistry


Under the Supervision of Dr. Ahmed Alzamly

November 2020

Declaration of Original Work

I, Salama Yousef Alismaail, the undersigned, a graduate student at the United Arab Emirates University (UAEU), and the author of this thesis entitled “*Synthesis, Characterization, Electronic Structure of BiOCl/BiOBr/rGO Ternary Heterojunction and its Photocatalytic Activities*”, hereby, solemnly declare that this thesis is my own original research work that has been done and prepared by me under the supervision of Dr. Ahmed Alzamly, in the College of Science at UAEU. This work has not previously been presented or published or formed the basis for the award of any academic degree, diploma or a similar title at this or any other university. Any materials borrowed from other sources (whether published or unpublished) and relied upon or included in my thesis have been properly cited and acknowledged in accordance with appropriate academic conventions. I further declare that there is no potential conflict of interest with respect to the research, data collection, authorship, presentation and/or publication of this thesis.

Student's Signature:



Date: 17-04-2021

Copyright © 2020 Salama Yousef Alismaail
All Rights Reserved

Advisory Committee

1) Advisor: Dr. Ahmed Alzamy

Title: Associate Professor

Department of Chemistry

College of Science

2) Co-advisor: Dr. Muna Bufaroosha

Title: Associate Professor

Department of Chemistry

College of Science

Approval of the Master Thesis

This Master Thesis is approved by the following Examining Committee Members:

- 1) Advisor (Committee Chair): Dr. Ahmed Alzamly

Title: Associate Professor

Department of Chemistry

College of Science

Signature



Date

04-04-2021

- 2) Member: Prof. Thies Thiemann

Title: Professor

Department of Chemistry

College of Science

Signature



Date

05-04-2021

- 3) Member (External Examiner): Prof. Ideisan Abu-Abdoun

Title: Professor

Department of Chemistry

Institution: University of Sharjah, United Arab Emirates

Signature



Date

12-04-2021

This Master Thesis is accepted by:

Dean of the College of Science: Professor Maamar Benkraouda

Signature Maamar Benkraouda Date May 26, 2021

Dean of the College of Graduate Studies: Professor Ali Al-Marzouqi

Signature Ali Hassan Date 26/5/2021

Copy ____ of ____

Abstract

Solar energy is free, most abundant among all renewable energy sources. Energy from the sun reaches the earth surface at a rate of 1.2×10^5 TW by far, exceeding the current world energy consumption of 17 TW ($1\text{TW} = 10^{12}$ J/s). Accordingly, development of visible light driven photocatalysts is of considerable interest in clean and renewable energy, as well as in wastewater treatment.

In that context, BiOCl and BiOBr and three different mole ratio composites were prepared, characterized using UV-vis DRS, PXRD, BET, SEM, and EDX and their photocatalytic activity for the photoreduction of 4-NA was evaluated. Results show that varying the mole ratio of BiOCl and BiOBr in the composites has no effect on the band gap energy. XRD patterns confirm the purity of the samples and SEM images show that pure BiOCl and BiOBr have a flake like morphology, However, prepared composites showed agglomerated particles. Moreover, BiOCl showed the lowest surface area of $3.30 \text{ m}^2/\text{g}$, compared to the prepared composites where BiOCl_{50%}/BiOBr_{50%} showed the highest surface area of $4.72 \text{ m}^2/\text{g}$. BiOCl_{75%}/BiOBr_{25%} presented higher photocatalytic activity compared to pure BiOCl and BiOBr indicating that the formation of a heterojunction facilitates electron transfer for photoreduction.

In addition, the highest photocatalytic activity of BiOCl_{75%}/BiOBr_{25%} was synthesized incorporating different rGO ratios. Results confirm the successful incorporation of rGO into the composite. Also, their photocatalytic activity was evaluated for the photoreduction of 4-NA, where composite of 5%rGO load exhibited the highest photocatalytic activity.

Keywords: Photocatalyst, Band gap, BiOCl, BiOBr, rGO, Composites.

Title and Abstract (in Arabic)

تحضير و توصيف و تحديد البنية الإلكترونية ل rGO/BiOBr /BiOCl ثلاثي التداخل ثم تحديد نشاطه كحافز ضوئي

الملخص

الطاقة الشمسية مجانية، وهي أكثر وفرة بين جميع مصادر الطاقة المتجددة. تصل الطاقة القادمة من الشمس إلى سطح الأرض بمعدل 1.2×10^5 TW. وهو ما يتجاوز استهلاك الطاقة العالمي الحالي البالغ 17 TW وبناء على ذلك فإن تطوير المحفزات الضوئية له أهمية كبيرة في الطاقة النظيفة والمتجددة، وفي معالجة مياه الصرف الصحي. في السنوات الأخيرة جذبت دراسة المحفزات الضوئية لأشباه الموصلات الكثير من الاهتمام نظراً لإمكانيتها في التطبيقات البيئية.

تم تحضير مركبات BiOBr و BiOCl ومركباتها ذات النسب المولية المختلفة وتم تمييزها باستخدام EDX و SEM و BET و PXRD و UV-vis DRS. ثم تم تقييم نشاطها الحفازي من خلال الاختزال الضوئي ل para-nitroaniline. أظهرت النتائج أن تغير النسب المولية لمركبات BiOBr و BiOCl ليس له تأثير على قيمة الفجوة الضوئية. أثبتت نتائج ال XRD نقاوة العينات المحضرة بالإضافة إلى نتائج ال SEM التي أظهرت أن BiOCl و BiOBr لديها شكل رقائق أما العينات المحضرة بنسب مختلفة فتمتلك شكل تراكب وتجمع جزيئات. أظهر مركب BiOCl أقل مساحة سطح بقيمة $3.30 \text{ m}^2/\text{g}$ أما المركبات المحضرة فأظهرت مساحة سطح أعلى حيث أن مركب $\text{BiOCl}_{50\%}/\text{BiOBr}_{50\%}$ أظهر مساحة سطح بقيمة $4.74 \text{ m}^2/\text{g}$. أما بالنسبة إلى النشاط الحفازي للمركبات أظهر مركب $\text{BiOCl}_{75\%}/\text{BiOBr}_{25\%}$ أعلى نشاط مما يشير إلى دور تكوين heterojunction الناجح في تسهيل عملية انتقال الإلكترونات لإكمال عملية الاختزال الضوئي.

بناءً على هذه النتائج تم تحضير ternary heterojunction باستخدام مركب ذو النسبة المولية $\text{BiOCl}_{75\%}/\text{BiOBr}_{25\%}$ و rGO لتحضير ثلاث مركبات بثلاث نسب كتل مختلفة من rGO. ثم تم اختبار نشاطها أيضاً لتفاعل اختزال مركب para-nitroaniline. تؤكد النتائج الدمج الناجح لـ rGO في $\text{BiOCl}_{75\%}/\text{BiOBr}_{25\%}$ على دور rGO في تقليل معدل إعادة التركيب، حيث يُظهر $\text{rGO} / \text{BiOCl}_{75\%}/\text{BiOBr}_{25\%} / 5$ أعلى نشاط حفاز ضوئي.

كلمات البحث الرئيسية: محفز ضوئي، فجوة النطاق، BiOCl، rGO، إعادة التركيب، BiOBr.

Acknowledgements

My first thanks go to Allah for providing me with this great opportunity and enabling me to seize it to get to where I am today.

Secondly, I would like to thank my committee for their guidance, support, and assistance throughout my preparation of this thesis, especially my advisor Dr. Ahmed Alzamly. For his full support throughout my master. I would like to thank the chair and all members of the Department chemistry at the United Arab Emirates University for assisting me all over my studies and research.

Special thanks go to my parents, brothers, and sisters for their prayers and full support along the way. I am sure they suspected it was endless. In addition, special thanks are extended to my husband for his big support.

Finally, to my research group Maram and Salwa for their assistance and friendship.

Dedication

To my beloved parents and family

Table of Contents

Title	i
Declaration of Original Work	ii
Copyright	iii
Advisory Committee	iv
Approval of the Master Thesis	v
Title and Abstract (in Arabic)	viii
Acknowledgements	ix
Dedication	x
Table of Contents	xi
List of Tables	xiii
List of Figures	xiv
List of Abbreviations	xvi
Chapter 1: Introduction	1
1.1 Semiconductors	1
1.2 TiO ₂ Photocatalyst	1
1.3 BiOX Structure	2
1.4 Heterojunction	3
1.5 Ternary Heterojunction	7
1.6 History and Synthesis of PPD	8
1.7 Aim of the Work	9
Chapter 2: Synthesis, Characterization, and Photocatalytic Activity of Pure BiOCl, BiOBr and their Binary Composites	10
2.1 Introduction	10
2.2 Materials and Methods	13
2.2.1 Materials	13
2.2.2 Synthesis of Pure BiOCl and BiOBr Photocatalysts	13
2.2.3 Synthesis of BiOCl/BiOBr Composites Photocatalysts	14
2.3 Characterization	14
2.3.1 Powder X-ray Diffraction (PXRD)	14
2.3.2 UV-Vis Diffuse Reflectance Spectroscopy (UV-Vis DRS)	14
2.3.3 Scanning Electron Microscopy (SEM) and Energy-Dispersive X-ray Spectroscopy (EDX)	15
2.3.4 Specific Surface Area and Porosity	15
2.3.5 Photocatalytic Activities	16
2.4 Results and Discussion	16
2.4.1 UV-Vis DRS for Pure BiOCl, BiOBr and Composites	16
2.4.2 PXRD Analysis for Pure BiOCl, BiOBr and their Composites	17

2.4.3 Scanning Electron Microscopy (SEM) Analysis and Energy-Dispersive X-ray (EDX) Analysis	19
2.4.4 BET Surface Analysis for Pure BiOCl, BiOBr and their Composites.....	23
2.4.5 Photocatalytic Activity of Pure BiOCl, BiOBr and their Composites.....	23
2.5 Proposed Mechanism	30
2.6 Conclusion.....	32
Chapter 3: Synthesis and Characterization of the Prepared Ternary System BiOCl/BiOBr/rGO and its Photocatalytic Activity for the Reduction of 4-Nitroaniline.....	33
3.1 Introduction	33
3.2 Materials and Methods	35
3.2.1 Materials	35
3.2.2 Synthesis of Reduced Graphene Oxide (rGO)	35
3.2.3 Synthesis of BiOCl/BiOBr/rGO Ternary Heterojunctions Photocatalysts	35
3.3 Characterization	36
3.4 Photocatalytic Activity.....	36
3.5 Results and Discussion.....	36
3.5.1 PXRD Analysis for BiOCl _{75%} /BiOBr _{25%} /rGO Composites	36
3.5.2 UV-Vis DRS for BiOCl _{75%} /BiOBr _{25%} /rGO Composites.....	37
3.5.3 BET Surface Analysis for BiOCl _{75%} /BiOBr _{25%} /rGO Composites.....	39
3.5.4 Morphology Characterization (SEM) and Elemental Analysis (EDX).....	40
3.5.5 Photocatalytic Activity of the BiOCl _{75%} /BiOBr _{25%} Composite and BiOCl _{75%} BiOBr _{25%} / rGO Ternary Composites	43
3.6 Conclusion.....	49
Chapter 4: Conclusion and Future Work	51
4.1 Conclusion.....	51
4.2 Further Studies	52
References.....	53

List of Tables

Table 1: Lattice parameters and physical properties for BiOCl, BiOBr and different BiOCl/BiOBr composites	18
Table 2: Weight and atomic percentage of pure BiOCl, BiOBr and their different BiOCl/BiOBr ratio composites	22
Table 3: Photocatalytic kinetics data for the reduction of 4-NA to PPD	30
Table 4: Lattice parameters for BiOCl _{75%} /BiOBr _{25%} and BiOCl _{75%} /BiOBr _{25%} /rGO composites	38
Table 5: Physical properties of BiOCl _{75%} /BiOBr _{25%} and BiOCl _{75%} /BiOBr _{25%} /rGO composites	39
Table 6: Atomic percentage of BiOCl _{75%} BiOBr _{25%} /rGO composites.....	43
Table 7: Weight percentage of BiOCl _{75%} BiOBr _{25%} /rGO composites.....	43
Table 8: Photocatalytic kinetics data for the reduction of 4-NA to PPD	45

List of Figures

Figure 1: Crystal structure of BiOCl. Color codes: Bi; purple, Cl; green, and O; red.....	11
Figure 2: Tauc plot for pure BiOBr and their different composites.....	17
Figure 3: Tauc plot for pure BiOCl.....	17
Figure 4: XRD pattern for the pure BiOCl, BiOBr and their different composites.....	18
Figure 5: SEM images for (a) BiOCl (b) BiOBr (c) BiOCl _{75%} /BiOBr _{25%} (d) BiOCl _{50%} /BiOBr _{50%} (e) BiOCl _{25%} /BiOBr _{75%}	20
Figure 6: EDX for (a) BiOCl (b) BiOBr (c) BiOCl _{75%} /BiOBr _{25%} (d) BiOCl _{50%} /BiOBr _{50%} (e) BiOCl _{25%} /BiOBr _{75%}	21
Figure 7: N ₂ adsorption-desorption isotherm of pure BiOCl, BiOBr and their BiOCl/BiOBr composites.....	23
Figure 8: Concentration variation of 4-NA over time under visible light irradiation in the presence of (a) pure BiOCl (b) pure BiOBr (c) BiOCl _{75%} /BiOBr _{25%} (d) BiOCl _{50%} /BiOBr _{50%} (e) BiOCl _{25%} /BiOBr _{75%} (f) NaBH ₄ and (g) TiO ₂ photocatalysts	25
Figure 9: Concentration variation of 4-nitroaniline over time using BiOCl, BiOBr, BiOCl/BiOBr composites, NaBH ₄ and TiO ₂ photocatalysts under visible light irradiation	28
Figure 10: Kinetics plot of $\ln C/C_0$ over time of pure BiOCl, BiOBr, BiOCl/BiOBr composites, NaBH ₄ and TiO ₂ photocatalysts.....	29
Figure 11: Calculated rate constants for BiOCl, BiOBr, BiOCl/BiOBr composites, NaBH ₄ and TiO ₂	29
Figure 12: Proposed mechanisms for the photocatalytic reduction of 4-NA to PPD.....	31
Figure 13: Reduced graphene oxide structure.....	34
Figure 14: XRD pattern for the prepared BiOCl _{75%} /BiOBr _{25%} and its three different rGO composites	37
Figure 15: Tauc plot for the prepared BiOCl _{75%} BiOBr _{25%} and BiOCl _{75%} BiOBr _{25%} /rGO composites	38
Figure 16: BET analysis for the prepared BiOCl _{75%} /BiOBr _{25%} and BiOCl _{75%} BiOBr _{25%} /rGO ternary composites	40
Figure 17: SEM images for (a) BiOCl _{75%} BiOBr _{25%} /1%rGO (b) BiOCl _{75%} BiOBr _{25%} /3%rGO and (c) BiOCl _{75%} BiOBr _{25%} /5%rGO.....	41

Figure 18: EDX of BiOCl _{75%} BiOBr _{25%} /rGO ternary composites	
(a) BiOCl _{75%} BiOBr _{25%} /1%rGO	
(b) BiOCl _{75%} BiOBr _{25%} /3%rGO and	
(c) BiOCl _{75%} BiOBr _{25%} /5%rGO.....	42
Figure 19: Concentration variation of 4-NA over time under visible light irradiation in the presence of	
(a) BiOCl _{75%} BiOBr _{25%} (b) BiOCl _{75%} BiOBr _{25%} /1%rGO	
(c) BiOCl _{75%} BiOBr _{25%} /3%rGO (d) BiOCl _{75%} BiOBr _{25%} /5%rGO	
(e) NaBH ₄ and (f) TiO ₂ photocatalysts.....	45
Figure 20: Concentration variation of 4-nitroaniline over time using BiOCl _{75%} BiOBr _{25%} , BiOCl/BiOBr/rGO composites, NaBH ₄ and TiO ₂ photocatalysts under visible light irradiation.....	48
Figure 21: Kinetics plot of $\ln C/C_0$ over time of BiOCl _{75%} BiOBr _{25%} , BiOCl/BiOBr/rGO composites, NaBH ₄ and TiO ₂ photocatalysts	49
Figure 22: Calculated rate constants for BiOCl _{75%} BiOBr _{25%} , BiOCl/BiOBr/rGO composites, NaBH ₄ and TiO ₂	49

List of Abbreviations

AO7	Acid Orange 7
BaSO ₄	Barium Sulfate
Bi(NO ₃) ₃ ·5H ₂ O	Bismuth (III) Nitrate Pentahydrate
BiOX	Bismuth Oxy Halide
BiOCl	Bismuth Oxy Chloride
BiOBr	Bismuth Oxy Bromide
BET	Brunauer-Emmett-Teller
BJH	Barett-Joyner-Halenda
BPA	Bisphenol A
CB	Conduction Band
CH ₃ COCH ₃	Acetone
CH ₃ COOH	Acetic Acid
DIW	Deionized Water
E _a	Activation Energy
EDX	Energy-Dispersive X-ray Spectroscopy
E _g	Band Gap
GO	Graphene Oxide
H ₂ O ₂	Hydrogen Peroxide
H ₂ SO ₄	Sulfuric Acid
KBr	Potassium Bromide
KCl	Potassium Chloride
KMnO ₄	Potassium Permanganate
MB	Methylene Blue

MO	Methyl Orange
4-NA	4- Nitro Aniline
NaBH ₄	Sodium Borohydride
NaNO ₃	Sodium Nitrate
N ₂ H ₄ .H ₂ O	Hydrazine Hydrate
PPD	Para-Phenylenediamine
PVP	Polyvinylpyrrolidone
PXRD	Powder X-ray Diffraction Spectroscopy
rGO	Reduced Graphene Oxide
RhB	Rhodamine B
SEM	Scanning Electron Microscopy
TiO ₂	Titanium Dioxide
UV-VIS DRS	UV-VIS diffuse Reflectance Spectroscopy
VB	Valence Band

Chapter 1: Introduction

1.1 Semiconductors

Using semiconductor materials as photocatalyst is an environment friendly alternative to control environmental pollution and low energy crises resulting from an increase in world population and modern industrialization [1], [2]. In order to achieve the best capability of photocatalysis, constructing a semiconductor photocatalyst with high efficiency and broad light absorption is gradually becoming a desirable target [3].

1.2 TiO₂ Photocatalyst

Since Fujishima and Honda discovered photocatalytic water splitting on n-type TiO₂ electrode using UV radiation and without applying an external voltage in an electrochemical cell, tremendous effort has been focused on developing more performing semiconductor materials [4], [5]. Until now, TiO₂ is well studied and has become a bench mark photocatalyst in the photocatalysis field [6] due to its characteristics such as: non-toxicity, abundance and cost effectiveness [7]. TiO₂ photocatalysts are broadly used in hazardous pollutant degradation, CO₂ conversion and water splitting [8]. However, TiO₂ suffers from the serious drawbacks of fast recombination rate and a large band gap of about ~3.3 eV indicating its absorption in the UV region which hinder its activity under visible light irradiation [9], [10], [11]. Worth noting, the solar spectrum is made of ~ 52% visible light, On the other hand, ultraviolet make up only 5% of the spectrum [12].

To date, numerous photocatalysts have been investigated as an alternative for TiO₂ [13] including metal and mixed metal oxides [14] such as ZnO [15], [16], CeO₂ [17], InTaO₃ [18], SrTiO₃ [19] and Ag₃VO₄ [20], [21].

Lately, bismuth-based photocatalysts have been reported, for instance, BiVO₄ [22], BiPO₄ [23], [24], Bi₂WO₆ [25], [26] and BiOX [27], [28]. Among bismuth based photocatalysts, BiOXs (X=Cl, Br, I) have drawn extreme interest because of their great ability to work as photocatalysts under UV and visible light radiations [29], [30]. moreover because of their unique crystal structure [31], chemical stability, corrosion resistance [32], non-toxicity [33] and abundance [34], their uses in many domains such as electronics [35], storage of energy [36], catalysis [37] and gas sensing [38] are well known.

1.3 BiOX Structure

BiOX structure is made up of covalently bonded tetragonal [Bi₂O₂]²⁺ slabs that are joined together by van der Waals interactions and where halogen atoms are found between these slabs. Thus the established internal static electric fields by the positive slabs and the negatively charged halogen atoms facilitate the photogenerated electron-hole pair separation [39], [40], [41], [42], [43].

Although BiOX has many interesting properties, there are some limitations due to its low photocatalytic efficiency [44] which does not meet the many needs of the market in its applications [45]. Therefore, developing new strategies to increase the photocatalytic activity are required.

1.4 Heterojunction

Many steps have been utilized to overcome the disadvantages of such photocatalysts [46], specially enhancing light absorption, encouraging the charge transfer and minimizing the recombination rate. For example, forming heterojunctions have been of huge attention due to the ability to promote electron-hole pair separation [47], [48], [49], [50], [51]. An example of such heterojunctions, $\text{BiOX}_1/\text{BiOX}_2$ ($X_1, X_2 = \text{Br, Cl, I and F}$) composites have been studied for many applications. Zhang *et al.* constructed flower-like $\text{BiOCl}/\text{BiOBr}$ microspheres using ionic liquids ($[\text{C16mim}]\text{Br}$) and ($[\text{C16mim}]\text{Cl}$) [52]. Compared to the pure BiOCl or BiOBr under visible light, $\text{BiOCl}/\text{BiOBr}$ microspheres exhibited enhancement in the photocatalytic removal of rhodamine B [52]. Huang *et al.* fabricated a multiple Heterojunction $\text{BiOBr}-\text{BiOI}$ photocatalyst leading to microstructure adjustment and adjustment of band structure using precipitation method. The photocatalytic activity was improved for the degradation of organic dyes and photocurrent generation for all the prepared heterojunctions [53]. Zhang *et al.* produced $\text{BiOCl}/\text{BiOBr}$ composite through microwave-assisted precipitation technique. The $\text{BiOCl}/\text{BiOBr}$ composite with a 1:5 ratio exhibited high photocatalytic activity even after five photocatalytic cycles indicating its high stability in decomposition of rhodamine B and better improvement in the visible light absorption [54]. Jiang *et al.* synthesized BiOBr/BiOF composites using the hydrothermal method. BiOBr/BiOF composites displayed an enhancement in photocatalytic activity compared to pure BiOBr in the degradation of nitrobenzene and rhodamine B under visible light irradiation [55]. Xu *et al.* produced a composite microsphere of BiOCl with BiOBr . The photoactivity of prepared composites was assessed through decomposition of rhodamine B. Results show that $\text{BiOCl}/\text{BiOBr}$

composite displayed much improvement in the photoactivity for rhodamine B decomposition and higher photocurrent intensity as compared to the pure and individual members of the composite [56]. Liu and co-workers fabricated 3D flower-like composite of BiOI/BiOX (X = Br or Cl). According to all of the prepared photocatalysts, BiOI/BiOCl can oxidize Methyl Orange (MO) efficiently under both irradiation by UV and visible light [57]. Wang *et al.* prepared 3D plasmonic Bi metal@defective BiOCl using the solvothermal method. (Bi/BiOCl-200) photocatalyst displayed optimal results for removing NO_x under visible light which is attributed to oxygen vacancies and Bi metal [58]. Aghdam *et al.* reported a nanocomposite of BiOI-BiOCl over g-C₃N₄ with a variety of ratios of BiOI and BiOCl using the precipitation method. The photocatalytic activity was investigated under visible light using the decomposition of Acid Orange 7 (AO7). Results indicated that the ratio (50) for BiOI-(30)for the BiOCl over 20g-C₃N₄ in the composite, displayed the best photocatalytic removal of AO7 and this is attributed to the ternary ability to promote the separation rate, reduce the photoinduced electron-hole pairs recombination and promote charge carriers [59]. Zhong *et al.* suggested an easy method to prepare BiOI/BiOCl films at room temperature. The photocatalytic performance was investigated through the degradation of both RhB and MB. The outcomes show that 30%BiOI/BiOCl efficiency is 5 and 12 times better than BiOI and BiOCl respectively, using the degradation of RhB, and 6 times in degrading of MB compared to BiOI. This is due to the high separation of charges and expanded absorption in the visible region. Moreover, recycling experiments showed that it can be recycled five times [60]. Cui *et al.* prepared BiOCl/BiOBr hybrid nanosheets using the alkaline hydrothermal method. Compared to pure BiOBr, the hybrid nanosheets exhibited outstanding photocatalytic activity which was ascribed to the uniform

allocation of BiOCl nanoparticles on BiOBr nanosheets leading to an increase in photoinduced carrier separation [61]. Wu *et al.* fabricated BiOX (X=Cl, Br, F, I) and different $x\text{BiOI}/(1-x)\text{BiOX}$ ($x=\text{F, Cl, or Br}$) composites by grinding dry powder of Bi_2O_3 and BiX_3 as starting materials [62]. The optical characterization and crystal phase structures of the samples were investigated using several methods. Results show that all prepared composites of BiOX exhibited a single phase and showed an improvement in the Bisphenol-A (BPA) degradation with the best efficiency at around 40%, using BiOI. Composite 0.5BiOI/ 0.5BiOCl show the optimal results as catalysts in BPA degradation. This was ascribed to good electron-hole pair separation [62]. Yang and co-workers constructed flower-like BiOBr/BiOCl composites among in-situ construction with KCl and ([AMIm]Br) ionic liquids. [AMIm]Br plays an important role as a source of Br and influencing the morphology of the composite. Moreover, BiOBr as a part of the composite speeds up the separation carriers' rate. Thus the BiOBr/BiOCl composite exhibited improvement in the photocatalytic activity which was more than six times of that of BiOCl [63]. Alzamyly *et al.* constructed BiOF/BiOI composite photocatalysts using the coprecipitation method. All prepared samples displayed enhancement in the photocatalytic activity towards removal of diclofenac potassium under the radiation of visible light [64]. Among all prepared photocatalysts 40% BiOF and 60% BiOI composite gave an optimal photocatalytic performance as compared to that of pure BiOI and BiOF [64]. Razavi-Khosroshahi *et al.* proposed a hydrothermal method to create different BiVO_4 with BiOX (X=Cl, Br, F, and I) p-n heterojunctions [65]. The methylene blue decomposition as contamination was used to assess the photocatalytic activity. The tests showed that the $\text{BiVO}_4/\text{BiOF}$ heterostructure has the optimal photocatalytic activity upon visible light irradiation which was attributed to the very low recombination rate according to the obtained

photoluminescence spectra [65]. Hu *et al.* prepared different p–n-heterojunction of $\text{Sn}_3\text{O}_4/\text{BiOX}$ ($X = \text{Cl}, \text{Br}, \text{I}$) using an ultrasonic-assisted precipitation–deposition method beside the hydrothermal strategy. $\text{Sn}_3\text{O}_4/\text{BiOCl}$ composite was the best in degrading rhodamine B (99%). $\text{Sn}_3\text{O}_4/\text{BiOX}$ ($X = \text{Cl}, \text{Br}$ and I) show better photocatalytic activity than bismuth oxyhalide and Sn_3O_4 individually because of the p-n heterostructure which indicates an improvement in the charge separation and an improved light absorption. Moreover, the high stability of the $\text{Sn}_3\text{O}_4/\text{BiOCl}$ composite was proved with four cycles of the RhB photodecomposition keeping the composite activity intact [66]. Maisang *et al.* synthesized a flower-like $\text{BiOBr}/\text{BiOCl}$ composite using a microwave-assisted hydrothermal method in different solutions consisting of (0-1) g Polyvinylpyrrolidone (PVP) [67]. Prepared composite morphology converted from microplates without PVP into micro flowers upon adding 1 g PVP. Under Xenon lamp irradiation, $\text{BiOBr}/\text{BiOCl}$ micro flowers exhibited optimum photocatalytic performance for the degradation of salicylic acid and rhodamine B [67]. Yao *et al.* proposed the BiOX/TiO_2 ($X = \text{Cl}, \text{Br}$ and I) hierarchical composites using solvothermal strategy and used it in the degradation of organic contamination in a short period [68]. Results show that the nanoparticles of TiO_2 as a cocatalyst increased in size on the BiOX nano sheets. $\text{BiOCl}/\text{TiO}_2$ show the best photocatalytic activity comparing to the other members of BiOX group. Moreover, the existence of columbite TiO_2 -II in anatase phase promote the separation of charge and visible light adsorption as a result improve the photocatalytic activity and tailored many characteristic of the composites such as: surface area and particle size [68].

1.5 Ternary Heterojunction

To date, many ternary heterojunctions have been constructed to motivate the photocatalytic activity [69]. For instance, Hassandoost *et al.* reported $\text{CeO}_2/\text{Fe}_3\text{O}_4/\text{GO}$ and $\text{Ce}^{3+}/\text{Fe}_3\text{O}_4/\text{GO}$ ternary heterojunctions and applied it for decontamination of oxytetracycline (OTC). The consolidation of small quantities of $(\text{Fe}_{3-x}\text{Ce}_x\text{O}_4/\text{GO}; x = 0.2)$ and ceria ($\text{Fe}_3\text{O}_4/\text{CeO}_2(0.7\%)/\text{GO}$) enhanced the harvesting of visible light and did not change the magnetic characteristic of magnetite or phase structure. Graphene oxide sheets play an important role by trapping electrons and expanding the photoinduced charge carriers' lifetimes, thus enhancing $\text{Fe}_{2.8}\text{Ce}_{0.2}\text{O}_4/\text{GO}$ photoactivity [70]. Li *et al.* fabricated BiOCl with both BiVO_4 and N-CD ternary composite for producing PEC sensor for the purpose of dopamine detection. $\text{BiOCl}/\text{BiVO}_4/\text{N-CD}$ heterojunction display high PEC performance compared to the binary composite $\text{BiOCl}/\text{BiVO}_4$, BiVO_4 and BiOCl individually [71].

Moreover, there are little reports on the investigation of ternary composites based on BiOX binary composites, Yuan *et al.* constructed BiOI and BiOBr with $\text{g-C}_3\text{N}_4$ ternary composites. The prepared composite exhibited higher photocatalytic performance for decomposition of methylene blue compared to $\text{g-C}_3\text{N}_4$ and BiOI/BiOBr . Moreover, 3% $\text{g-C}_3\text{N}_4/\text{BiOI}/\text{BiOBr}$ display the optimal photocatalytic activity. Combination of $\text{g-C}_3\text{N}_4/\text{BiOI}/\text{BiOBr}$ gives synergistic effect according to charge transfer procedure [72]. Accordingly, ternary heterojunction can make improvement in the photocatalytic performance because their capability to promote photogenerated electron-hole pairs separation.

1.6 History and Synthesis of PPD

The first implementation of Para-Phenylenediamine (PPD) was in 1863 for the formation of an azo dye, later it was used for the synthesis of organic dyes [73]. PPD has many industrial applications [74] such as, dyes [75], rubber antioxidants [76], pharmaceuticals [77], aramid textile fibers [78] and thermoplastics [79]. Catalytic hydrogenation of 4-nitroaniline (4-NA) is a widespread method to produce PPD [80]. Nonetheless, these operations face considerable drawbacks of strict reaction conditions [81], demanding procedures [82] and high cost [83]. Therefore, constructing an environmentally friendly, low cost and non-hazardous strategy for the synthesis of PPD is needed.

Conventionally, 4-nitroaniline reduction is carried out catalytically in the existence of H₂ and metals as catalyst [84]. For instance, Bawane and co-workers studied the catalytic conversion of *p*-nitroaniline to (PPD) using 5% of the catalyst (Pd/C) [85]. Farooqi *et al.* investigated the conversion of 4-nitroaniline catalytically in the presence of nanoparticles of Ag constructed in microgels that work as catalyst due to their expanded structure [86]. Das *et al.* studied the removal of 4-nitroaniline using catalytic reduction in the existence of RGO–Ni nanocomposite as a catalyst [87]. Naseem *et al.* reported the catalytic reduction of 2-nitroaniline using various reducing agents such as hydrazine hydrate and sodium borohydride [88]. Edison and co-workers proposed the reduction of *p*-nitroaniline through (Ag NPs) with NaBH₄ [89].

Using semiconductors as photocatalysts for organic conversions have been expanded over the past decade [90]. However, semiconductors with wide band gap like TiO₂ limited light absorption only to the UV region [91]. UV is small compared

to the abundant visible light percentage [92]. So, constructing photocatalysts with visible light responsive for organic transformations is desirable.

Recently the conversion of 4-nitroaniline to *p*-phenylenediamine in aqueous solution using photocatalysis have great focus from researchers. For instance, Imamura *et al.* proposed using TiO₂ photocatalysts for the photoconversion of 4-NA to PPD in aqueous solution containing formic acid as a hole scavengers [93]. Wu *et al.* proposed the utilizing of In₂S₃ photocatalyst for the photoreduction of 4-NA with the existence of triethanolamine which act as hole scavenger [94]. Moreover, Wu and co-workers studied the photocatalytic conversion of 4-nitroaniline using SrBi₂Nb₂O₉ photocatalyst. The enhanced photocatalytic activity was ascribed to its high conduction band [95]. Also, constructed by sol gel method PbBi₂Nb₂O₉ photocatalyst for the same purpose [96].

1.7 Aim of the Work

BiOCl/BiOBr composites with various ratios will be studied and prepared by coprecipitation method. Also, the impact of rGO on the prepared binary composites will be investigated by forming ternary heterojunction of BiOCl/BiOBr/rGO. The as prepared photocatalysts will be characterized through using UV-Vis Diffuse Reflectance Spectroscopy (UV-Vis DRS), Powder X-ray Diffraction (PXRD), Scanning Electron Microscopy (SEM), Brunauer-Emmett-Teller (BET), and Energy-Dispersive X-ray Spectroscopy (EDX). The photocatalytic activity of the pure BiOCl, BiOBr, BiOCl/BiOBr and BiOCl/BiOBr/rGO composites photocatalysts will be examined for the reduction of 4-nitroaniline as a model reaction.

Chapter 2: Synthesis, Characterization, and Photocatalytic Activity of Pure BiOCl, BiOBr and their Binary Composites

2.1 Introduction

Bismuth-oxy halides considered as an outstanding materials for the energy photoconversion [97] and environment-remediation [98]. BiOX (X=Cl, Br, and I) attracted great attention from researchers due to their special structure [99] and its implementations in many domains such as, secondary batteries [100], gas sensors [101] and solar cells [102]. However, the most significant purpose is as photocatalysts that apply in decontamination of dangerous organic or inorganic pollutants such as methyl orange [103], tetrabromobisphenol A [104] and the poisonous gas NO [105].

In 1935, Bannister clarified bismuth-oxy halides structure which is composed of tetragonal matlockite type [106] which consist of [X–Bi–O–Bi–X] slabs connected to each other by the forces of Van der Waals spreading through the halogen atoms as presented in Figure 1 showing the crystal structure of BiOCl where X= Cl in this case [107]. Every slab contains Bi atom, four oxygen and four halogen atoms which the Bi atom surrounding by the oxygen and the halogen atoms. The internal static field which constructed perpendicular to the slabs improve the charge separation and minimize the recombination rate [108]. Crystal structure was drawn using crystalmaker program and atomic coordination is found in reference [109].

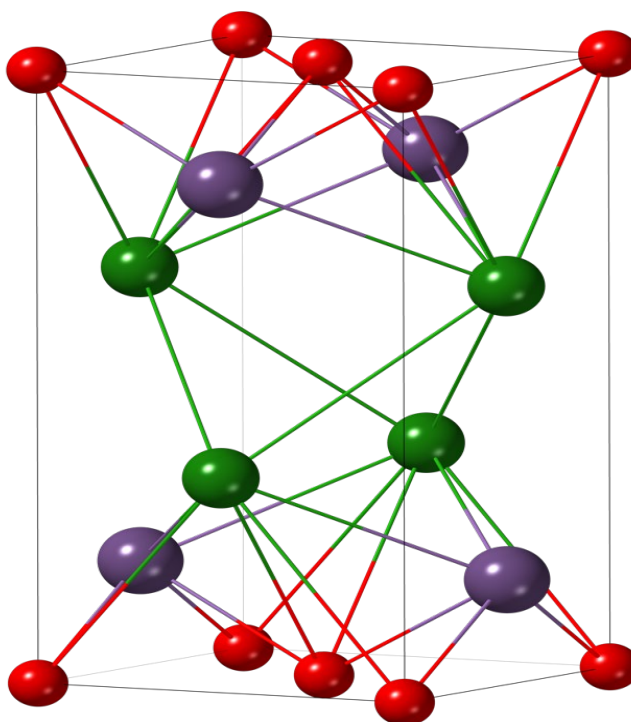


Figure 1 : Crystal structure of BiOCl. Color codes: Bi; purple, Cl; green, and O; red

Various strategies have been used for the BiOX synthesis [110]. For example, Zhang *et al.* suggested achievable way for the fabrication of hierarchical BiOX nanoplate microspheres by using ethylene glycol as solvent using solvothermal technique. The photoactivity of the nanoplates were assessed according to the degradation of methyl orange and comparing its activity with TiO₂ under UV and visible light radiation. Results found that BiOI has the best photocatalytic activity under UV and visible light radiation because it has appropriate band gap (1.77 eV) [111]. An and co-workers synthesized BiOX (X = Cl, Br, and I) via a hydrolysis way. The enhanced photocatalytic activity of BiOX was evaluated under visible light irradiation for the photo decontamination of rhodamine B. Results show that the best result obtained on degradation of rhodamine B using BiOBr [112]. Lei *et al.* prepared 2D plate like BiOCl and 3D hierarchical BiOCl structure by a sonochemical method. Accordingly, the 2D nanoplate can be obtained at low energy and short time around

30 minutes. This 2D nanoplate can be converted by using surfactant reagents to 3D hierarchical structure. Moreover, the photocatalytic activity of the obtained nanoplates was investigated using degradation of methene orange dye which show that the 3D hierarchical structure enhances the photocatalytic activity [113].

Bismuth oxychloride considered as a photocatalyst used in the removal of pollutants but its wide band gap (3.6 eV) reduce its photocatalytic activity [114]. On the other hand, BiOBr with the band gap of approximately (2.9 eV) gives it good photocatalytic activity under both UV and visible light irradiation [115]. Thus forming heterojunction with narrow band gap semiconductor can improve the electron-hole pairs separation and promote light absorption to a lower band gap, thus increase the photoactivity [116].

To achieve excellent photocatalytic system, it should characterized by several properties such as, suitable band gap (1.6–2.2 eV), high sunlight harvesting, good mobility, and corrosion resistance during reaction conditions [117]. However, it is hard to meet all these properties using one photocatalyst. So, heterojunctions appeared as a promising method to achieve all these requirements.

To date, forming heterojunctions through a combination between more than one material such as two semiconductors based on band alignment have been developed to improve the capability of charge separation and maximize the light absorption efficiency [118]. Heterojunctions can make acceleration of the charge separation and increase the range of light absorption [119].

Many binary heterojunctions show improvement in the photocatalytic activity compared with the single one [120]. For instance, Ma and co-workers Prepared

BiOBr/BiOCl flower-like composite using hydrothermal method in the existence of [BP_y]Br which play an important role in the maximizing charge separation and improve the surface area as well as considered as a source of Br. Results confirm that the composite has better photoactivity compared to the single BiOCl [121]. Zhao and co-workers fabricated microspheres of BiOBr/BiOCl through solvothermal technique. The composite indicated higher photoactivity comparing with the pure BiOCl or BiOBr [122]. Zhang *et al.* produced by hydrothermal approach an assembled BiOCl/BiOBr nanosheet in the presence of ethylene glycol. Experimental results displayed improvement in the photoactivity performance comparing with the pure component in decomposition of methylene blue [123]. Liu *et al.* prepared a heterojunction with high oxygen vacancies of BiOCl with BiOBr by using photoinduced with ultrasound technique [124].

2.2 Materials and Methods

2.2.1 Materials

Bismuth(III) nitrate pentahydrate (Bi(NO₃)₃·5H₂O), potassium bromide (KBr), potassium chloride (KCl), acetic acid (CH₃COOH, 99.7%), acetone (CH₃COCH₃), ethanol(C₂H₅OH), Sodium borohydride (NaBH₄), 4-nitroaniline (H₂NC₆H₄NO₂), and hydrazine hydrate (N₂H₄·H₂O) were purchased from Sigma Aldrich and used without further purification.

2.2.2 Synthesis of Pure BiOCl and BiOBr Photocatalysts

BiOCl was synthesized using coprecipitation technique using the following steps: 9.7 g of Bi (NO₃)₃·5H₂O was dissolved in 150 mL 4 M acetic acid with constant stirring and heating at 80°C. KCl solution was prepared as: 1.49 g of KCl was

dissolved in 10 mL of deionized water. After that KCl solution was added dropwise to $\text{Bi}(\text{NO}_3)_3 \cdot 5\text{H}_2\text{O}$ solution with stirring. The resulting white product formed, reaction let to stir for 8 h at room temperature then collected by filtration, washed several times with DI water and ethanol. BiOCl was dried at 80°C in an oven for 2 h then calcined at 400°C for 2 h. Same steps was applied for the synthesis of BiOBr by using (KBr, 2.38 g). the product was dried in an oven at 80°C for 2 h followed by calcination at 150°C for 2 h.

2.2.3 Synthesis of $\text{BiOCl}/\text{BiOBr}$ Composites Photocatalysts

Different composites have been prepared according to a simple mechanical mixing of the two pure powders. For example, the composite $\text{BiOCl}_{50\%}/\text{BiOBr}_{50\%}$ has been prepared as follows: 50 mol% BiOCl was mixed with 50 mol% BiOBr in a Porcelain Pestle using 10 mL acetone followed by strong mixing until the homogenous mixture of the powders completely dried. Same steps were applied for the preparation of the remaining composites denoted as $\text{BiOCl}_{25\%}/\text{BiOBr}_{75\%}$, and $\text{BiOCl}_{75\%}/\text{BiOBr}_{25\%}$.

2.3 Characterization

2.3.1 Powder X-ray Diffraction (PXRD)

PXRD was performed using a Shimadzu-6100 powder XRD diffractometer with $\text{Cu-K}\alpha$ radiation with working voltage 40 kV and current 40 mA where $\lambda=1.542 \text{ \AA}$. The diffraction data was scanned in the 2θ angle range of $10\text{--}60^\circ$ at a rate of $2^\circ/\text{min}$.

2.3.2 UV–Vis Diffuse Reflectance Spectroscopy (UV–Vis DRS)

UV–Vis diffuse reflectance spectroscopy (UV–Vis DRS) analysis was collected using a Shimadzu UV-3600 UV–Vis spectrophotometer in the wavelength range from

200 to 800 nm. BaSO₄ have been used for baseline correction as a reference standard. the spectra gives results about the band gap energies using the Tauc Plot method [125]. considering that these photocatalysts were direct semiconductors and using Equation (1).

where α , E_g , h , ν , A , n being the absorption coefficient, band gap, Planck's constant, frequency of light, a constant and the number characterizing transition for direct/indirect semiconductor materials ($n=1/2$ for allowed direct transitions) respectively [126].

$$(\alpha h\nu)^{\frac{1}{n}} = A(h\nu - E_g) \quad (1)$$

According to this equation the Band gap values were obtained from the plotted graph of $(\alpha h\nu)^2$ vs. $(h\nu)$.

2.3.3 Scanning Electron Microscopy (SEM) and Energy-Dispersive X-ray Spectroscopy (EDX)

A FEI SEM Quanta Inspect S50 Scanning electron microscope equipped with EDS-Oxford INCA PENTA at a voltage of 30 Kv was applied to determine the morphology and elemental compositions. The samples were placed in a holder fixed with carbon tape after a coating process with gold.

2.3.4 Specific Surface Area and Porosity

Quantachrome Autosorb-1 volumetric gas sorption instrument was used for characterization of Surface area and porosity using N₂ adsorption at 77 K. Before measurements, samples were degassed at 150°C for 2 hours to calculate surface area

Brunauer-Emmett-Teller (BET) theory was applied, and the pore size were determined by Baret-Joyner-Halenda (BJH) model.

2.3.5 Photocatalytic Activities

The photocatalytic activity of the pure BiOCl, BiOBr and BiOCl/BiOBr composite photocatalysts was assessed through the photocatalytic reduction of 4-nitroaniline as a model reaction. A solution of 4-nitroaniline (1×10^{-4} M) was prepared, and 100 mL from the (1×10^{-4} M) solution was transferred into 250 mL round flask, then 100 mg of the photocatalyst was added to the solution under constant stirring for 10 mins, N_2 gas was purged inside the solution. the solution was positioned around 15 cm from the source of light which is 500 W Halogen lamp (OSRAM HALOLINE), with wavelength from 380 to 780 nm. As a reducing agent 3 mg of $NaBH_4$ was added to the solution at chosen time intervals. and 3 mL of the reaction solution was collected, filtered, and measured for UV-Vis absorption analysis.

2.4 Results and Discussion

2.4.1 UV-Vis DRS for Pure BiOCl, BiOBr and Composites

Figure 2 and Figure 3 demonstrate the Tauc plots of the UV-VIS DRS spectra of the pure BiOCl, BiOBr and BiOCl/BiOBr composites photocatalysts. Pure BiOCl and BiOBr show a direct allowed band gap of 3.32 eV and 2.92 eV respectively. To reduce the band gap of BiOCl it was mixed with BiOBr with different mole ratios. However, the different prepared composites BiOCl_{25%}/BiOBr_{75%}, BiOCl_{50%}/BiOBr_{50%} and BiOCl_{75%}/BiOBr_{25%} showed close band gap range of 3.00 eV, 2.80 eV, and 2.85 eV respectively.

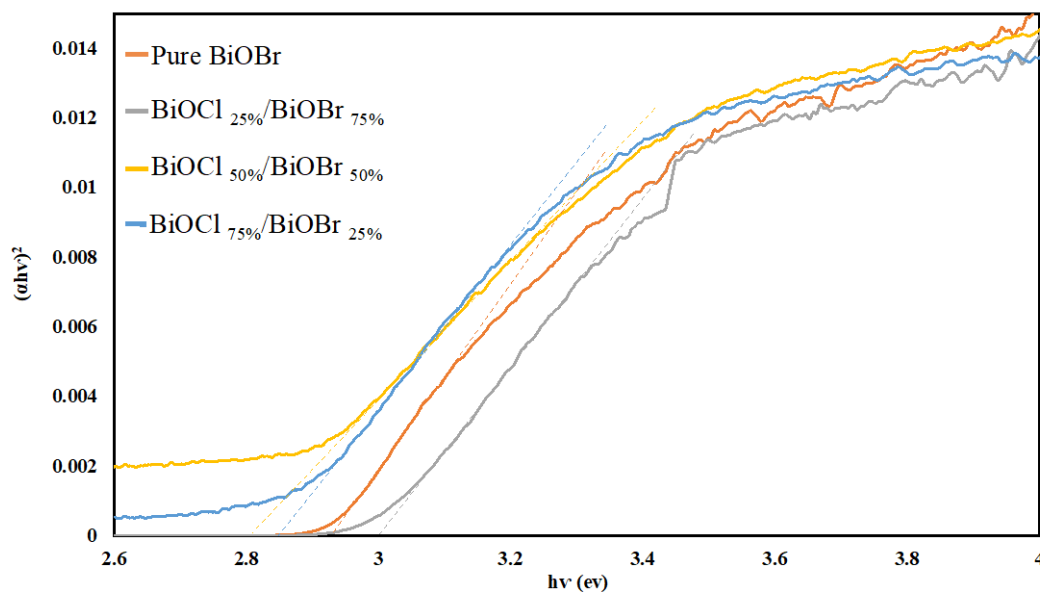


Figure 2: Tauc plot for pure BiOBr and their different composites

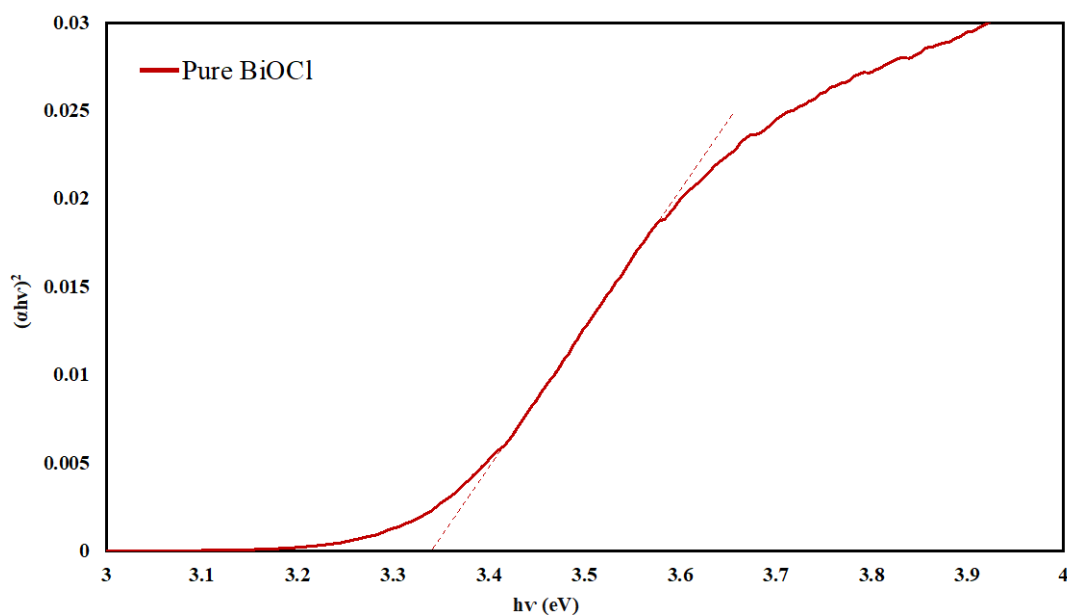


Figure 3: Tauc plot for pure BiOCl

2.4.2 PXRD Analysis for Pure BiOCl, BiOBr and their Composites

PXRD patterns for the prepared pure BiOBr and BiOCl and their different mole ratios composites are presented in Figure 4. Pure BiOBr and BiOCl diffraction peaks are perfectly indexed to the tetragonal lattice structure (JCPDS file No. 78-0348) and (JCPDS No: 09-0393) respectively. As for the composites they exhibit combination of

both diffraction peaks of BiOBr and BiOCl with no extra peaks for any impurities. Diffraction peaks for BiOCl at $2\theta = 12.02, 24.24, 25.94, 32.56, 33.52, 36.72, 41.00, 46.66, 49.80, 54.16, 55.22, 58.72, 60.94$ and 68.22 were indexed for (001), (002), (101), (110), (102), (003), (112), (200), (004), (211), (104), (212), (203) and (220) respectively. Moreover, BiOBr peaks appears at $2\theta = 10.86, 21.98, 25.18, 31.70, 32.24, 39.34, 46.24, 47.76, 50.74, 53.38, 56.24$ and 57.12 and are indexed to (001), (002), (101), (102), (110), (112), (200), (113), (104), (211), (114) and (212) planes respectively. The intensity of the main peak for BiOCl at $2\theta = 25.94$ increase as its molar ratio increase in the composites along with all peaks that corresponds to BiOCl where remnant peaks intensity for BiOBr decrease. All calculated lattice parameters are shown in Table 1.

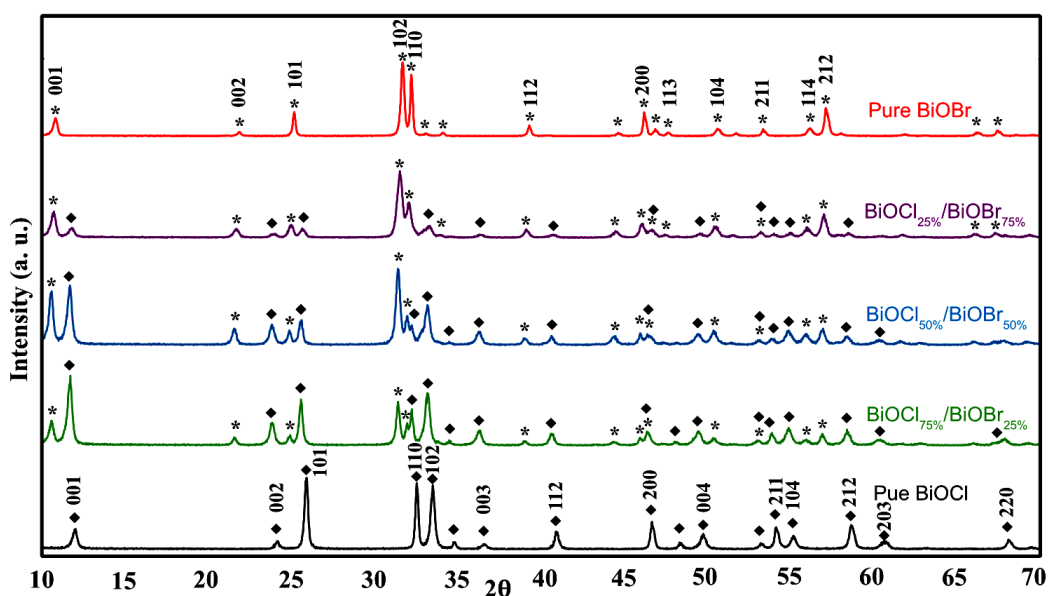


Figure 4: XRD pattern for the pure BiOCl, BiOBr and their different composites

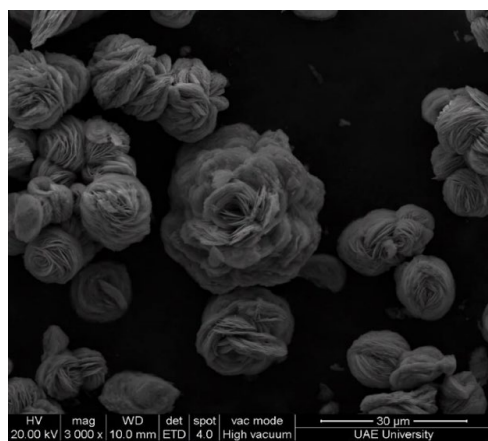
Table 1: Lattice parameters and physical properties for BiOCl, BiOBr and different BiOCl/BiOBr composites

Sample	Lattice parameters					Pore size (nm)	Surface area (m ² /g)	Band gap (eV)
		a=b	C	V (Å ³)	$\alpha=\beta=\gamma$			
Pure BiOCl	BiOCl	3.89	7.33	110.69	90	102.93	3.30	3.32
BiOCl _{75%} /BiOBr _{25%}	BiOCl	3.91	7.53	115.33	90	102.55	3.98	2.85
	BiOBr	3.94	8.32	129.53				
BiOCl _{50%} /BiOBr _{50%}	BiOCl	3.91	7.53	115.33	90	108.18	4.72	2.80
	BiOBr	3.85	8.32	123.52				
BiOCl _{25%} /BiOBr _{75%}	BiOCl	3.90	7.43	113.23	90	97.06	3.96	3.00
	BiOBr	3.94	8.22	127.62				
Pure BiOBr	BiOBr	3.90	8.17	124.20	90	111.20	3.70	2.92

2.4.3 Scanning Electron Microscopy (SEM) Analysis and Energy-Dispersive X-ray (EDX) Analysis

The SEM images were used to examine the morphology of the pure BiOCl, BiOBr and BiOCl/ BiOBr composites Figure 5. Both pure BiOCl and BiOBr exhibit same flake-like morphology Figure 5a, b. On the other hand, the composites do not show any distinctive morphology where they exhibit agglomerated particles.

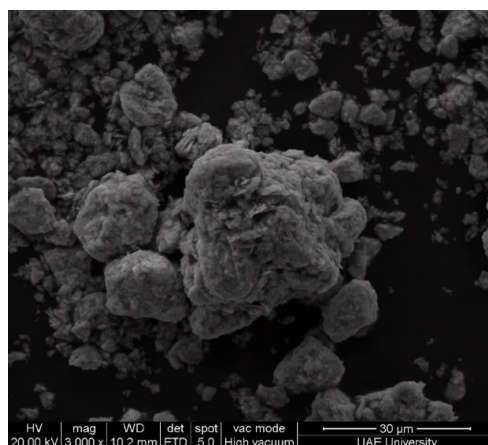
EDX was used to determine the elemental composition of the prepared photocatalysts. Figure 6 confirms the existence of Bi, O, Cl, and Br with no extra peaks proving the purity of the samples. Table 2 present the atomic and weight percent of each element, the data show that as percent Cl increase in the composites its atomic and weight percent increases and Br decreases as its mole ratio decrease which confirms the successful preparation of the different mole ratio composites.



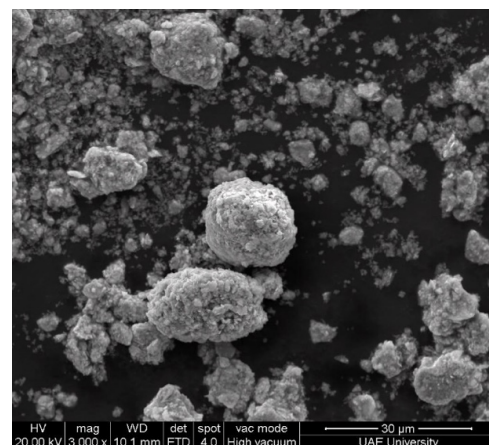
(a)



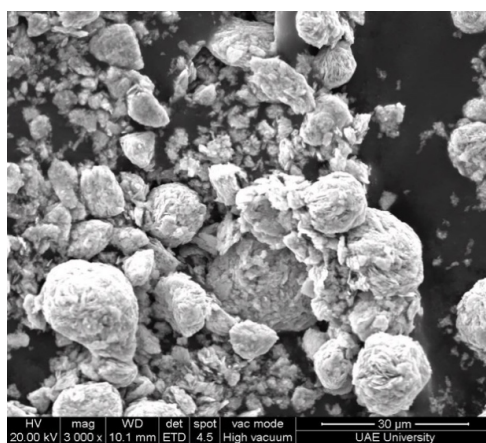
(b)



(c)

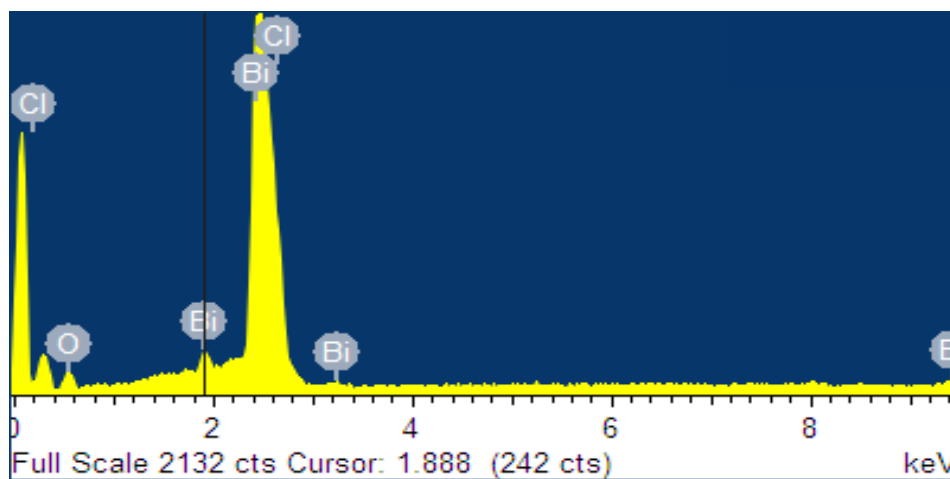


(d)

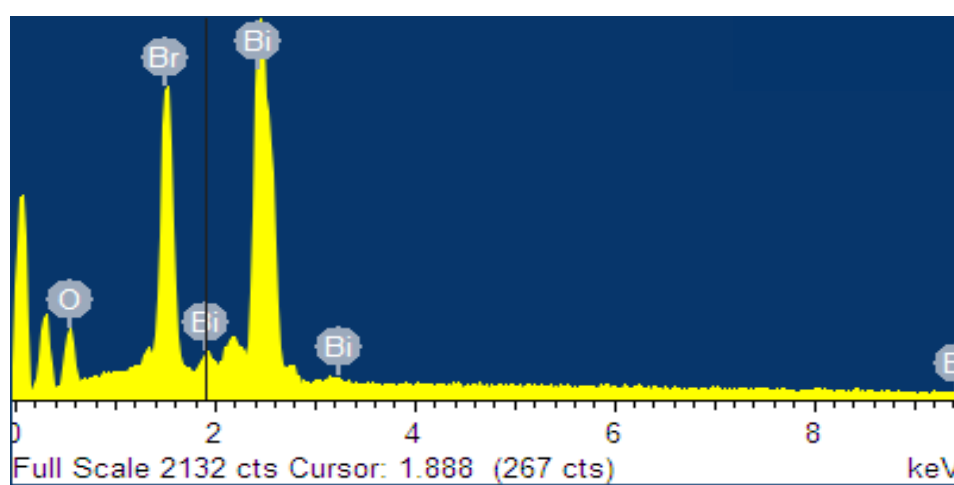


(e)

Figure 5: SEM images for (a) BiOCl (b) BiOBr (c) BiOCl_{75%}/BiOBr_{25%} (d) BiOCl_{50%}/BiOBr_{50%} (e) BiOCl_{25%}/BiOBr_{75%}



(a)



(b)

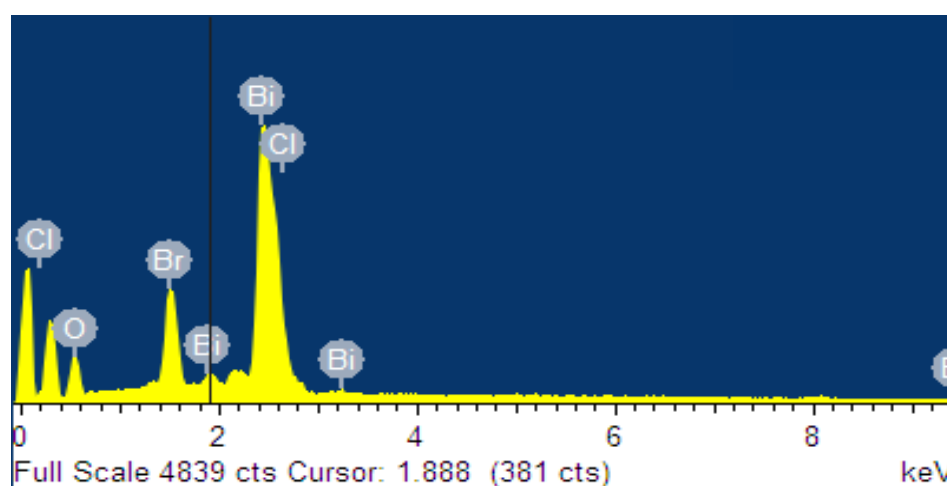
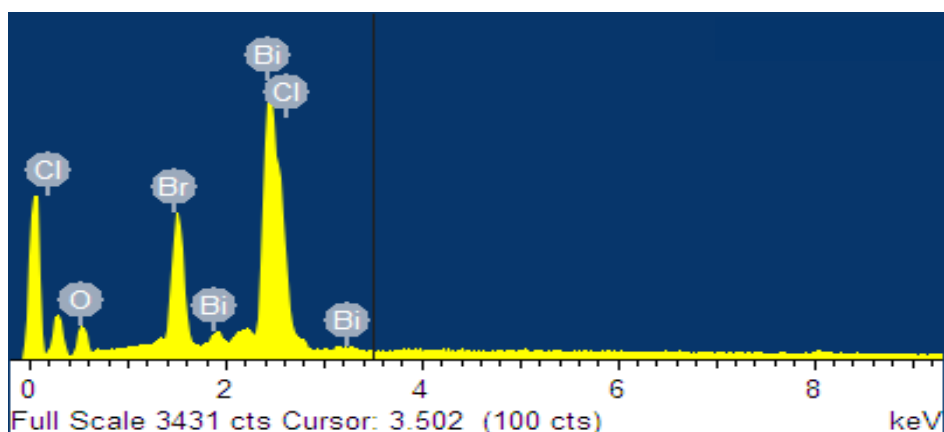
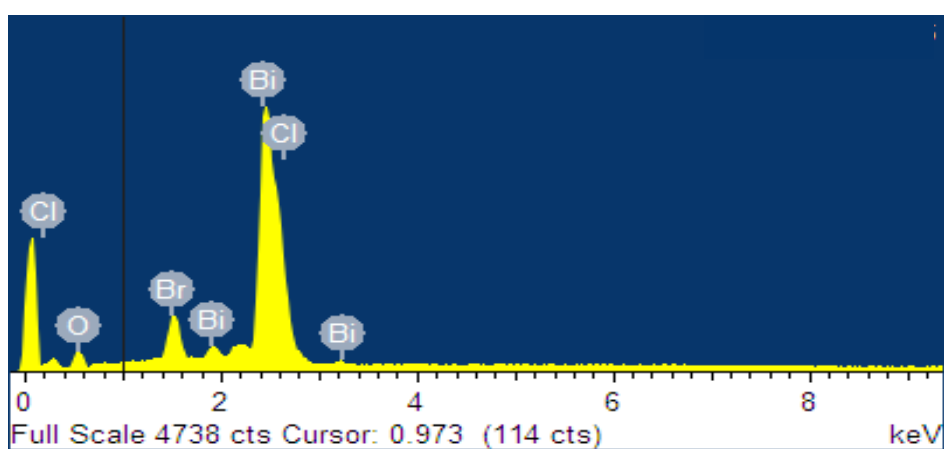


Figure 6: EDX for (a) BiOCl (b) BiOBr (c) BiOCl_{75%} /BiOBr_{25%} (d) BiOCl_{50%} /BiOBr_{50%} (e) BiOCl_{25%} /BiOBr_{75%}



(d)



(e)

Figure 6: EDX for (a) BiOCl (b) BiOBr (c) BiOCl_{75%} /BiOBr_{25%} (d) BiOCl_{50%} /BiOBr_{50%} (e) BiOCl_{25%} /BiOBr_{75%} (continued)

Table 2: Weight and atomic percentage of pure BiOCl, BiOBr and their different BiOCl/BiOBr ratio composites

Samples	Weight %				Atomic %			
	O	Bi	Cl	Br	O	Bi	Cl	Br
Pure BiOCl	15.41	74.37	10.22	-	59.92	22.14	17.94	-
BiOCl _{75%} /BiOBr _{25%}	9.34	75.66	7.28	7.73	46.79	29.01	16.45	7.75
BiOCl _{50%} /BiOBr _{50%}	17.38	64.93	4.34	13.35	64.41	18.43	7.26	9.91
BiOCl _{25%} /BiOBr _{75%}	13.29	66.50	2.35	17.86	57.74	22.12	4.62	15.53
Pure BiOBr	11.33	66.31	-	22.37	54.24	24.31	-	21.44

2.4.4 BET Surface Analysis for Pure BiOCl, BiOBr and their Composites

The Brunauer–Emmett–Teller (BET) specific area of pure BiOCl, BiOBr and BiOCl/BiOBr composites was evaluated according to N₂ adsorption-desorption isotherm analysis. Figure 7 reveals that prepared photocatalyst has hysteresis loop in the range of 0.75-1.0 P/P₀ with III isotherm type. As shown in Table 1, the surface area of pure BiOCl and BiOBr is 3.3037 m²/g and 3.6909 m²/g respectively. Calculated surface area for the prepared composites is higher than the pure BiOBr and BiOCl, no trend was observed for the increase in surface area, whereas BiOCl_{50%}/BiOBr_{50%} showed the highest surface area of 4.7219 m²/g.

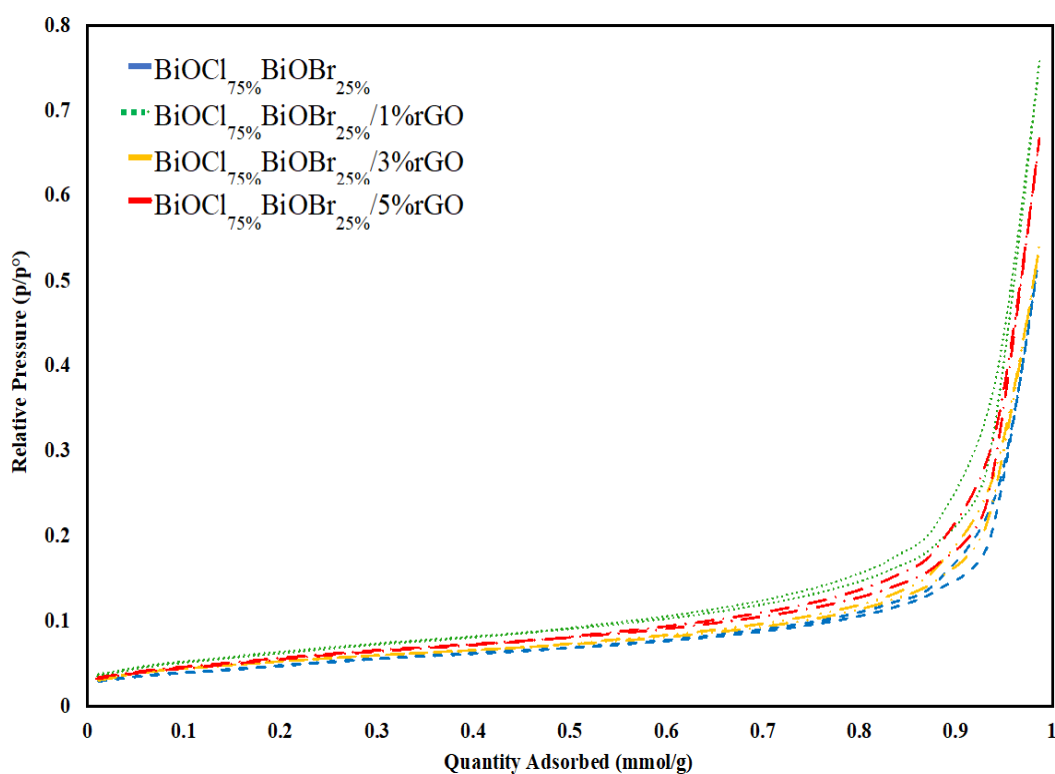


Figure 7: N₂ adsorption-desorption isotherm of pure BiOCl, BiOBr and their BiOCl/BiOBr composites

2.4.5 Photocatalytic Activity of Pure BiOCl, BiOBr and their Composites

The photocatalytic activity of the prepared pure BiOCl, BiOBr and their three

different mole ratio composites was examined for the photoreduction of 4-Nitroaniline (4-NA) to *p*-Phenylenediamine (PPD) using NaBH₄ as reducing agent. The absorption was measured at certain time intervals while irradiating the reaction under visible light for 30 min to observe the change in the characteristic peak for 4-NA at 380 nm. As shown in Figure 8 all photocatalysts exhibited a decrease at 380 nm a combined with the appearance for two extra peaks at 283 nm and 305 nm that corresponds to the formation of PPD as irradiation time increases. Table 3 present the calculated rate constants for the prepared photocatalysts. Pure BiOCl show the lowest k constant value of 0.11 min⁻¹ because of its wide band gap, whereas BiOBr showed a higher k constant value of 0.20 min⁻¹, such observation could be attributed to the lower band gap of BiOBr compared to BiOCl. As for prepared composites they exhibited higher photocatalytic activity proving the successful construction of the heterojunction between BiOCl and BiOBr forming efficient transfer for electrons for the photoreduction of 4-NA. BiOCl_{75%}/BiOBr_{25%} showed the highest calculated rate constant of 0.29 min⁻¹ with conversion percent of 99.4%. Another two reactions were conducted using NaBH₄ to understand its role in the reaction and TiO₂ as a benchmark photocatalyst in the field. As observed in Figure 8f, g the reaction was kept for 130 min and no complete conversion was observed, proving that NaBH₄ act as a reducing agent and the reaction needs a photocatalyst to be completed. As for TiO₂ it has a wide band gap making it more active in the UV region explaining its low activity in the visible region.

Figure 9 displays the relationship between C/C_0 over 20 min for the prepared pure photocatalysts and the composites. the graph clearly shows the difference in the performance for NaBH₄, TiO₂ and the other prepared photocatalysts, also it shows that

prepared composites outstand the photocatalytic activity of pure BiOCl. Figure 10 confirms that the reaction follows first order kinetics for the conversion of 4-NA to PPD, where straight lines were observed for the obtained experimental data upon drawing the variation of $\ln(C/C_0)$ as a function of time (20 min). Calculated rate constants for the photoconversion reaction are reported in Figure 11.

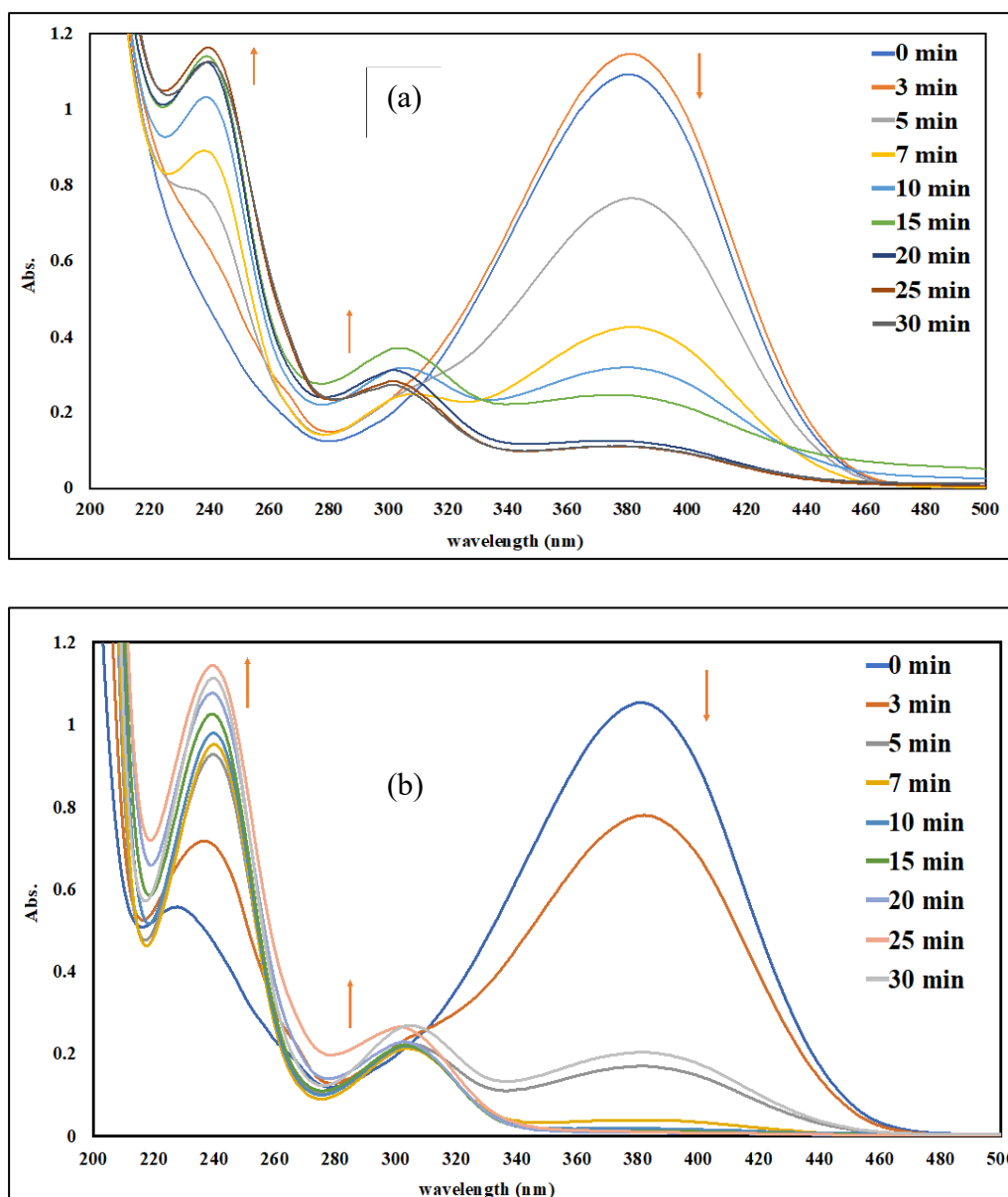


Figure 8: Concentration variation of 4-NA over time under visible light irradiation in the presence of (a) pure BiOCl (b) pure BiOBr (c) BiOCl_{75%} /BiOBr_{25%} (d) BiOCl_{50%} /Bi-OBr_{50%} (e) BiOCl_{25%} /BiOBr_{75%} (f) NaBH₄ and (g) TiO₂ photocatalysts

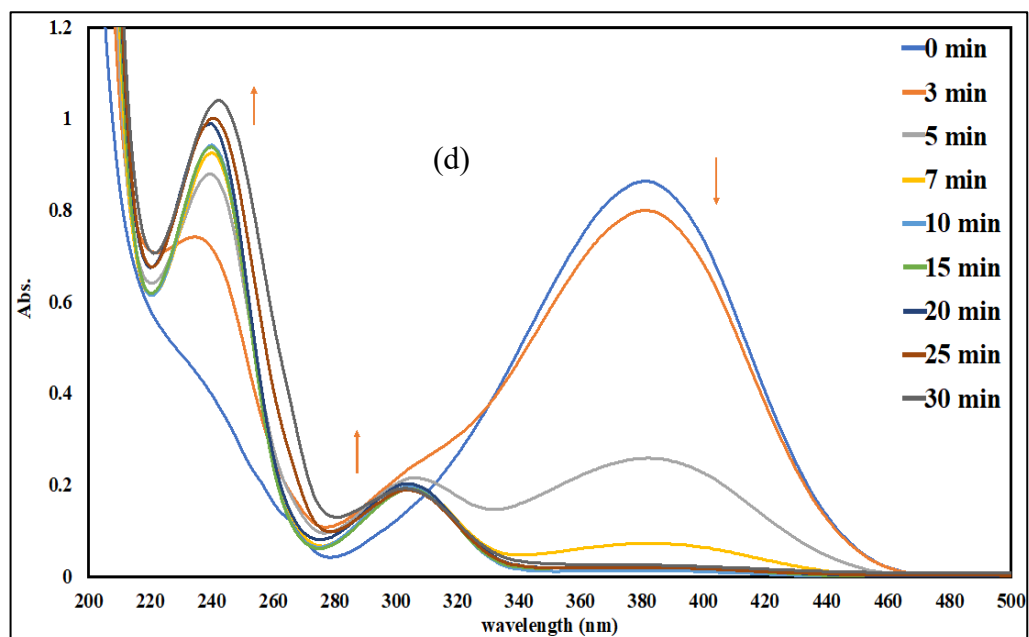
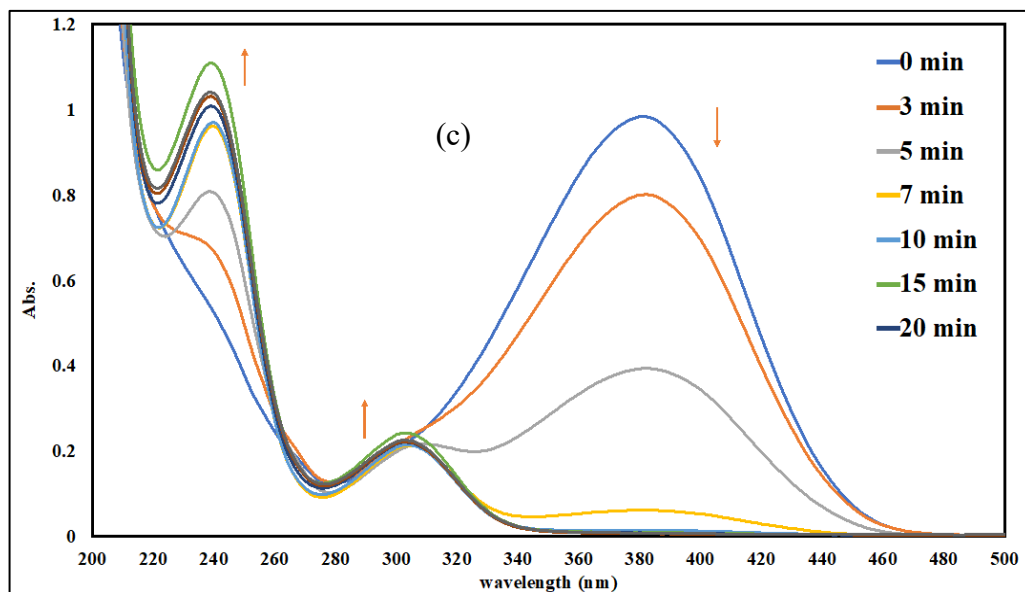


Figure 8: Concentration variation of 4-NA over time under visible light irradiation in the presence of (a) pure BiOCl (b) pure BiOBr (c) BiOCl_{75%} /BiOBr_{25%} (d) BiOCl_{50%} /BiOBr_{50%} (e) BiOCl_{25%} /BiOBr_{75%} (f) NaBH₄ and (g) TiO₂ photocatalysts (continued)

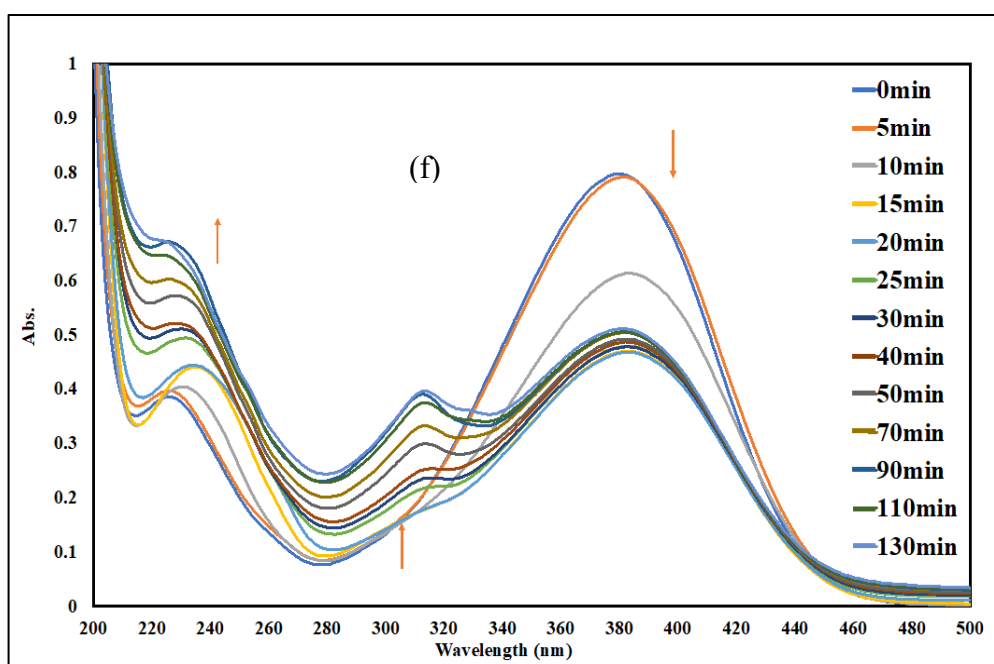
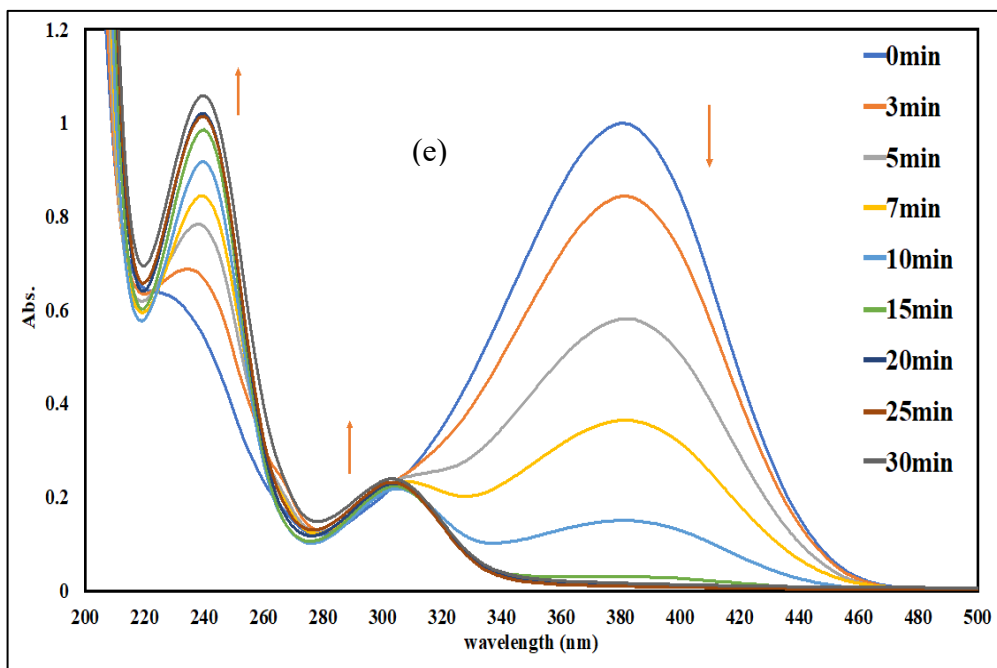


Figure 8: Concentration variation of 4-NA over time under visible light irradiation in the presence of (a) pure BiOCl (b) pure BiOBr (c) BiOCl_{75%} /BiOBr_{25%} (d) BiOCl_{50%} /BiOBr_{50%} (e) BiOCl_{25%} /BiOBr_{75%} (f) NaBH₄ and (g) TiO₂ photocatalysts (continued)

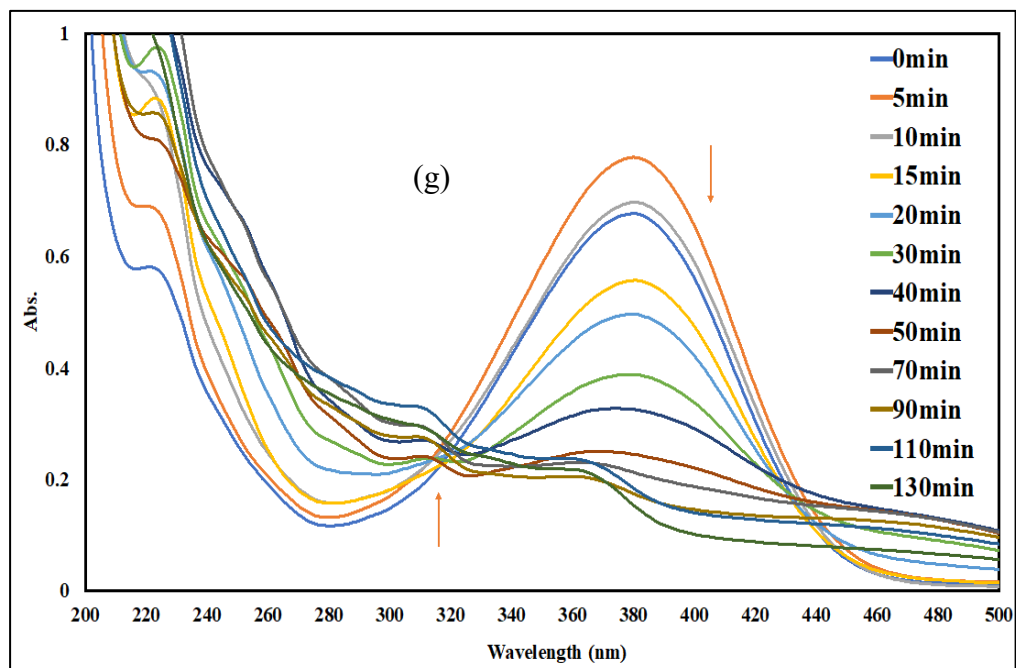


Figure 8: Concentration variation of 4-NA over time under visible light irradiation in the presence of (a) pure BiOCl (b) pure BiOBr (c) BiOCl_{75%}/BiOBr_{25%} (d) BiOCl_{50%}/BiOBr_{50%} (e) BiOCl_{25%}/BiOBr_{75%} (f) NaBH₄ and (g) TiO₂ photocatalysts (continued)

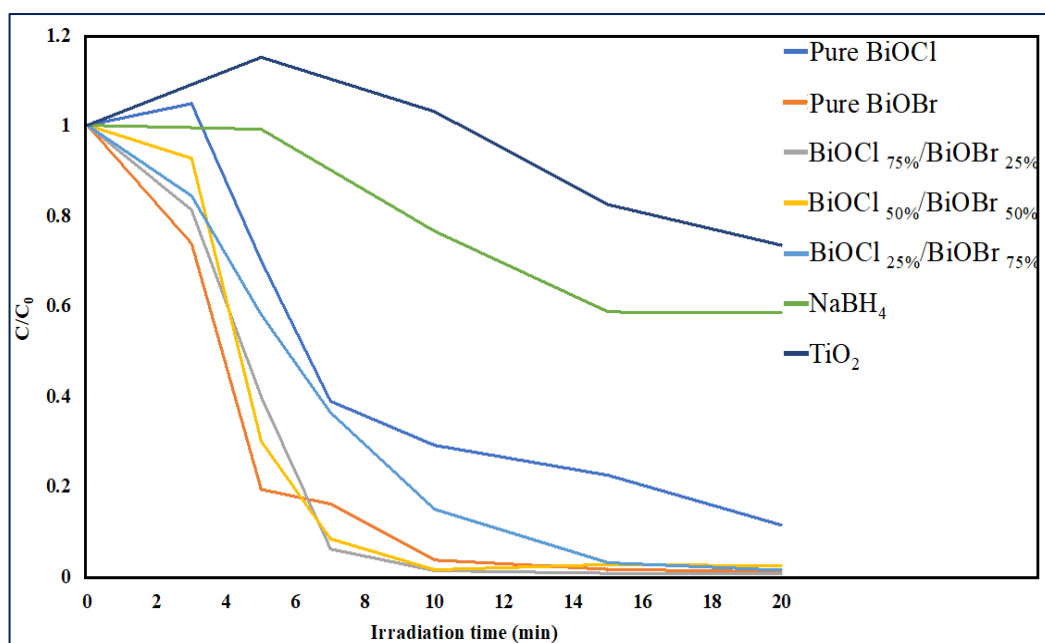


Figure 9: Concentration variation of 4-nitroaniline over time using BiOCl, BiOBr, BiOCl/BiOBr composites, NaBH₄ and TiO₂ photocatalysts under visible light irradiation

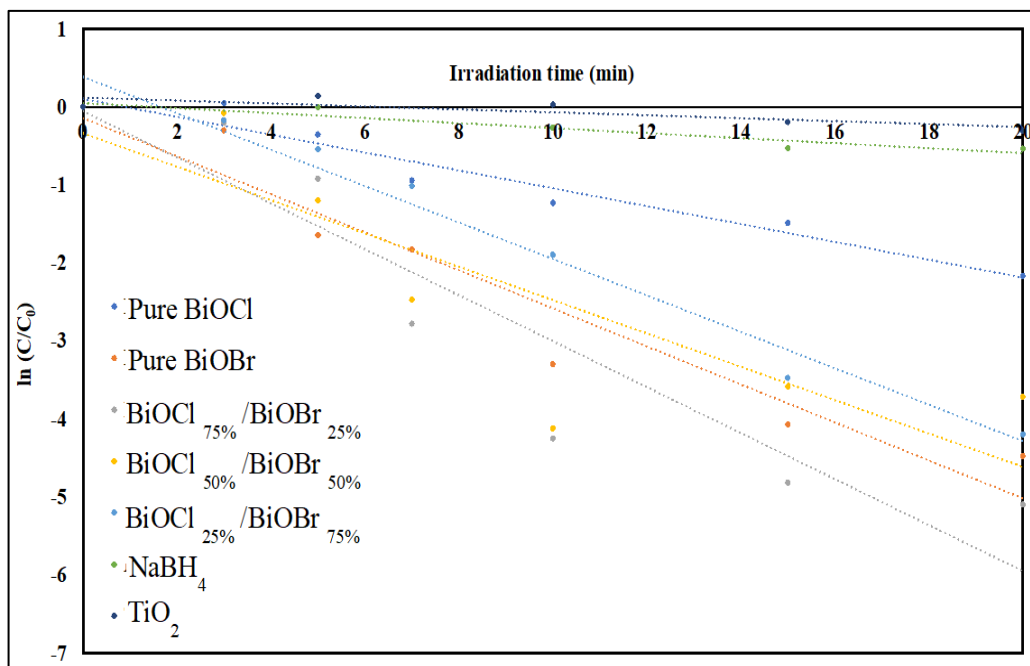


Figure 10: Kinetics plot of $\ln C/C_0$ over time of pure BiOCl, BiOBr, BiOCl/BiOBr composites, NaBH₄ and TiO₂ photocatalysts

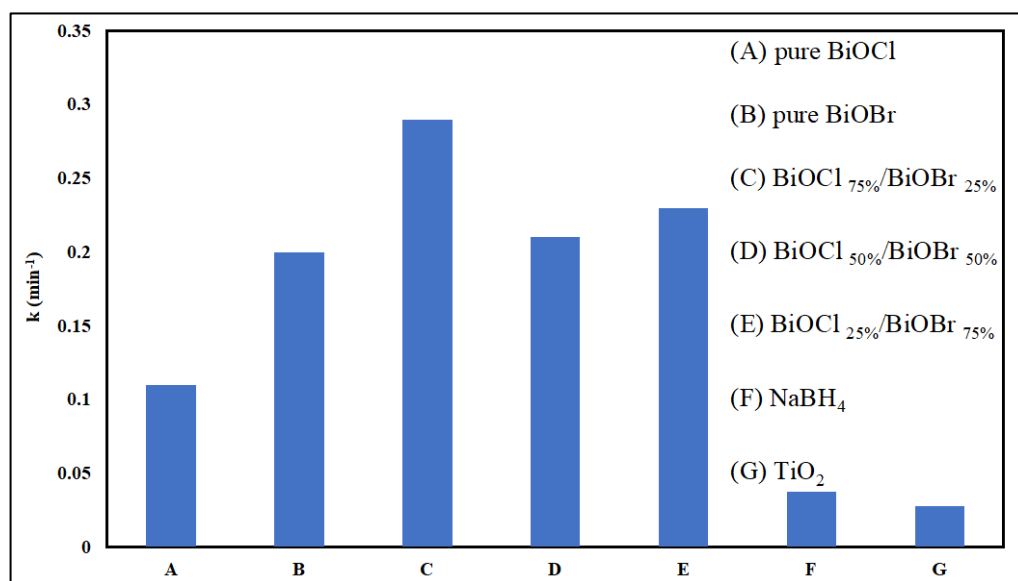


Figure 11: Calculated rate constants for BiOCl, BiOBr, BiOCl/BiOBr composites, NaBH₄ and TiO₂

Table 3: Photocatalytic kinetics data for the reduction of 4-NA to PPD

Photocatalyst	K (min ⁻¹)	Conversion (%) after 20 min
Pure BiOCl	0.11	88.6
Pure BiOBr	0.20	98.9
BiOCl _{75%} /BiOBr _{25%}	0.29	99.4
BiOCl _{50%} /BiOBr _{50%}	0.21	97.6
BiOCl _{25%} /BiOBr _{75%}	0.23	98.5
NaBH ₄ without photocatalyst	0.038	41.3
TiO ₂	0.028	17.6

2.5 Proposed Mechanism

Due to the availability of excited electrons (e^-) in the Conduction Band (CB) of the photocatalyst and electron holes (h^+) in the Valence Band (VB) the reduction of 4-NA could proceed through two processes. The first one could be either by the OH radicals generated from water by the excited e^- in the CB or through reduction by electron holes (h^+) on active sites of the photocatalyst. So, the mechanism as follows when the photocatalyst get excited, electrons move from the VB to CB leaving behind electron holes (h^+). Then excited electrons reduce water molecules generating OH radicals that react with 4-NA to reduce it to PPD. The other mechanism involves the adsorption of 4-NA on the active sites of the photocatalyst and reduce it through electron holes (h^+) to PPD as presented in Figure 12.

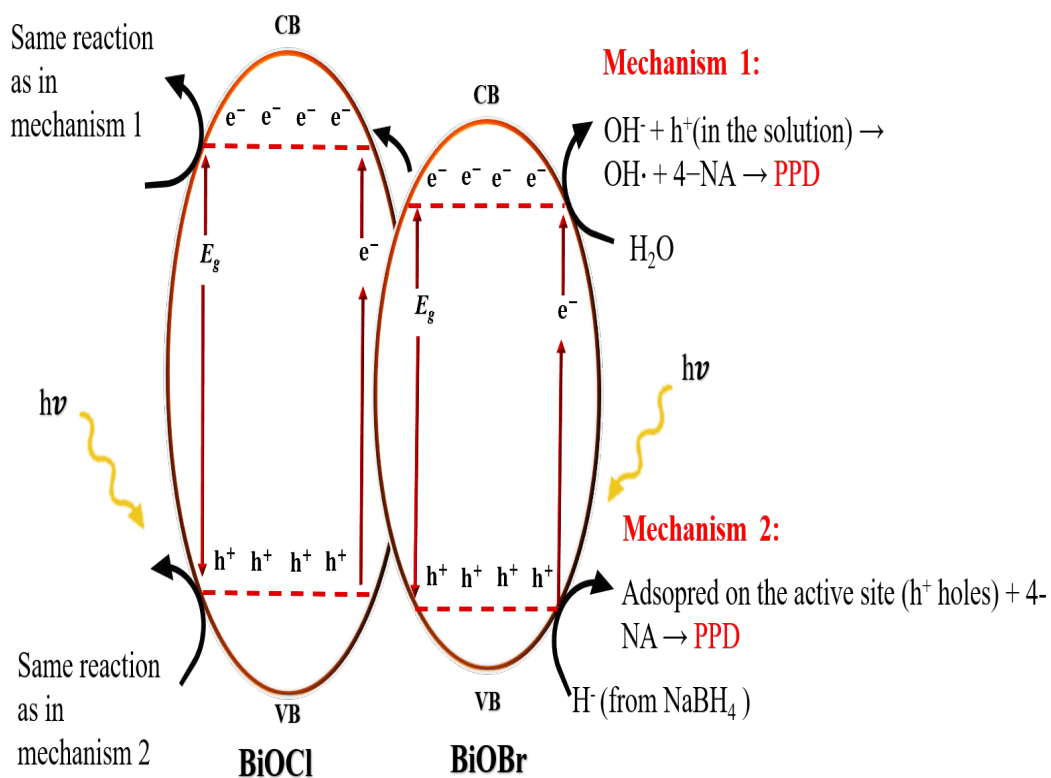
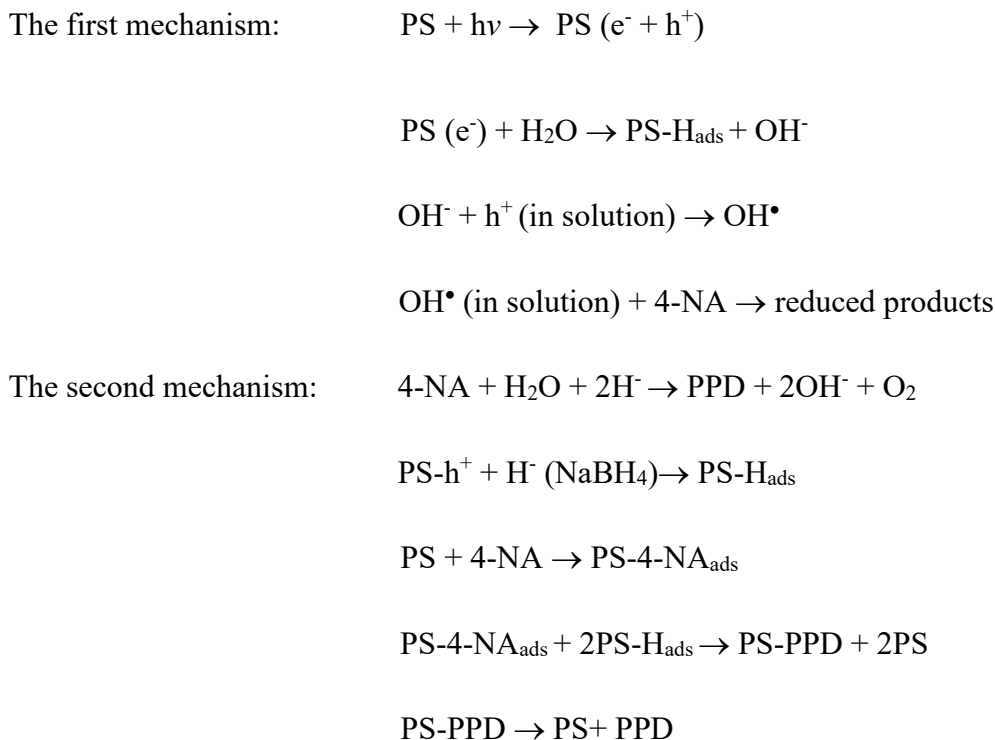


Figure 12: Proposed mechanisms for the photocatalytic reduction of 4-NA to PPD

2.6 Conclusion

In conclusion, BiOCl and BiOBr and their composites were prepared successfully, characterized and their photocatalytic activity for the photoreduction of 4-NA was evaluated. Different mole ratio composites exhibited almost the same band gap value where varying the mole ratio of BiOCl and BiOBr in the composites did not affect the band gap energy. XRD patterns confirm the purity of the samples with no extra peaks that would show any impurities. Pure BiOCl and BiOBr showed a flake like morphology however, prepared composites showed agglomerated particles. Moreover, BiOCl showed the lowest surface area of 3.30 m²/g, and prepared composites exhibited higher surface area where BiOCl_{50%}/BiOBr_{50%} showed the highest surface area of 4.72 m²/g. BiOCl_{75%}/ BiOBr_{25%} presented higher photocatalytic activity as compared to pure BiOCl and BiOBr, indicating that the formation of a heterojunction facilitates electron transfer for photoreduction.

Chapter 3: Synthesis and Characterization of the Prepared Ternary System BiOCl/BiOBr/rGO and its Photocatalytic Activity for the Reduction of 4-Nitroaniline

3.1 Introduction

Since the revolution of graphene began in 2004 and until now this 2D sheet of carbon atoms gained incredible interest due to its amazing characteristics [127] that includes high surface area [128], the ability to absorb almost all the regions in the light spectrum [129], physical and chemical stability [130], and outstanding electron mobility [131]. Graphene based materials attracts great attention due to their numerous applications owing to their optical, mechanical, and electrical features [132].

The conversion of Graphene Oxide (GO) to Reduced Graphene Oxide (rGO) can be accomplished by the chemical reduction of GO using reducing agents such as, ascorbic acid [133], sodium borohydride [134] and hydrazine hydrate [135]. The Reduced graphene oxide structure consists of epoxy, hydroxy, and carboxylic acid groups distributed randomly along the edge and the plane of the carbon sheet (Figure 13) [136]. The incredible properties that are mentioned above for the rGO give it an important role in photocatalysis as a support to enhance the capability of such photocatalyst [137]. Moreover, rGO has the ability to promote the charge transfer to improve the separation of electron hole [138] and minimize the recombination rate [139].

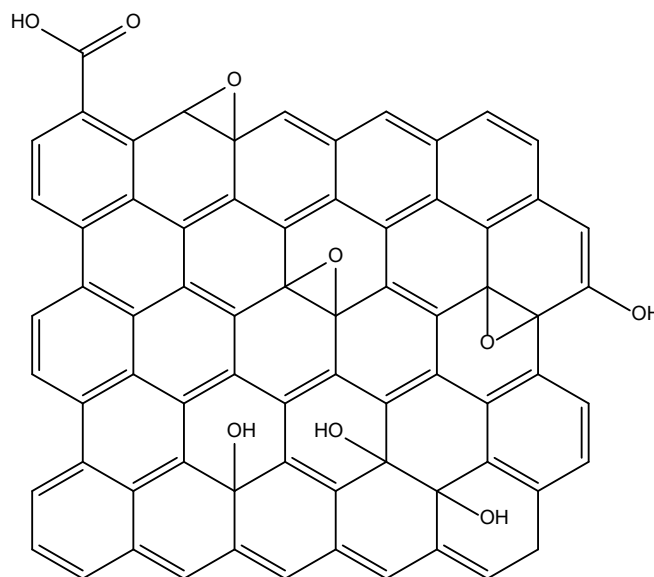


Figure 13: Reduced graphene oxide structure

Nowadays the interest focuses on the formation of composites consisting of carbon material with other material to improve the properties of such composite [140]. For example, Pan *et al.* synthesized nanocomposites of BiOBr with Bi₄O₅Br₂ and rGO with stacked nanosheets using solvothermal strategy. The results confirmed that rGO has an important role in improving the separation capability of photoinduced carriers and promotes the decontamination effectiveness of ciprofloxacin [141]. Pramoda *et al.* reported enhanced photocatalytic performance of C₃N₄ with layers of MoS₂ and nitrogenated rGO ternary heterojunction and attributed the effective separation of photogenerated charge carriers the internal electric field built by nitrogenated rGO interlayers [142]. Zhang *et al.* reported Ternary Z-Scheme Heterojunction of Bi₂WO₆ with rGO and Bi₂₅FeO₄₀ with enhanced photocatalytic activity due to the effective charge separation, better light absorption and large surface area [143]. Accordingly, ternary heterojunctions have an advantage of efficient separation of photogenerated electron-hole pairs due to the synergistic effect of multi-component heterojunction.

It was reported in this Chapter the synthesis, characterization, and photocatalytic activity of BiOCl/BiOBr/rGO ternary heterojunction photocatalysts for the photocatalytic reduction of 4-NA in aqueous solution.

3.2 Materials and Methods

3.2.1 Materials

Graphite powder (100+ mesh), sulfuric acid (H₂SO₄), Sodium nitrate (NaNO₃), Hydrogen peroxide (H₂O₂), hydrazine hydrate (N₂H₄·H₂O), Potassium permanganate (KMnO₄). were purchased from Sigma Aldrich and used as received without further purification.

3.2.2 Synthesis of Reduced Graphene Oxide (rGO)

rGO was prepared by mixing 2 g Graphite powder and 0.12 g NaNO₃ in 60 mL sulfuric acid, the mixture was kept in ice bath with stirring for 1 h. 6 g of KMnO₄ were added gradually to the mixture under constant stirring for 1 h. Then 60 mL Deionized Water (DIW) were added to the mixture. The temperature was increased to 90°C and held constant for 30 min. Then 200 mL of (DIW) was added to the solution, followed by the addition of 30 mL H₂O₂. GO was obtained then filtered and washed with 2 M HCl and DI water and dried in 100°C oven. Dried GO was mixed with DI water and 5 mL of hydrazine hydrate to reduce GO to rGO, then filtered and dried for 1 day in the oven.

3.2.3 Synthesis of BiOCl/BiOBr/rGO Ternary Heterojunctions Photocatalysts

BiOCl_{75%}/BiOBr_{25%} composite and rGO were prepared as described in Section (2.2.3) and Section (3.2.2) respectively. The composites were prepared with four mass

ratios 1%, 3%, 5% and 10%. For instance, BiOCl/BiOBr/1% rGO composite was prepared by mixing 1.09 g composite and 0.01 g rGO in 10 mL acetone followed by strong mixing until the added acetone evaporated and the homogenous mixture completely dried. Then the product was placed in an oven for 2 days at 150°C. Same steps were applied for the other different rGO ratio composites using 1.09 g BiOCl_{75%}/BiOBr_{25%} with 0.03 g, 0.05 g and 0.1 g rGO respectively.

3.3 Characterization

Same characterization methods were applied as described in Chapter 2, Section 2.3.

3.4 Photocatalytic Activity

Same reaction conditions were implemented as in Chapter 2, Section 2.3.5.

3.5 Results and Discussion

3.5.1 PXRD Analysis for BiOCl_{75%}/BiOBr_{25%}/rGO Composites

The prepared BiOCl_{75%}/BiOBr_{25%} exhibited both diffraction peaks for BiOCl and BiOBr as shown in Figure 14 that matches (JCPDS file No. 78-0348) and (JCPDS No: 09-0393) database respectively. Pure prepared rGO has a broad peak at 26.3°, therefore in the prepared ternary system of BiOCl_{75%}/BiOBr_{25%}/rGO a small shoulder peak appears at one of the main peaks of BiOCl at 25.94°. The low intensity of the peak is attributed to the low content of rGO in the prepared three different composites. All prepared composites exhibited diffraction peaks attributed to BiOCl, BiOBr and rGO with no extra peaks for any impurities. Prepared composites exhibited a slight ~ 0.5° shift to lower diffraction angles indicating expansion of the unit cell

based on Bragg's law.

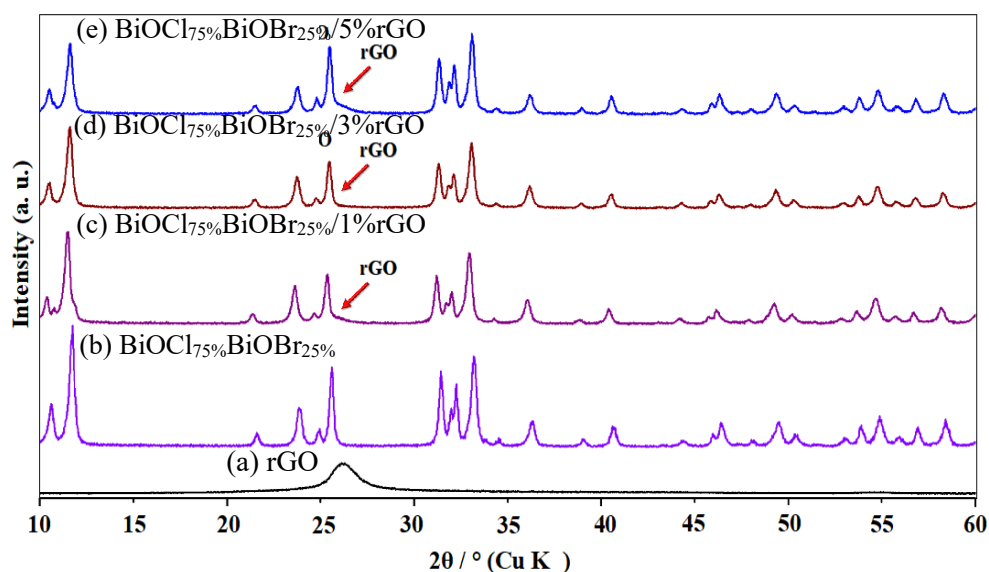


Figure 14: XRD pattern for the prepared BiOCl_{75%}/BiOBr_{25%} and its three different rGO composites

3.5.2 UV-Vis DRS for BiOCl_{75%}/BiOBr_{25%}/rGO Composites

Based on the obtained results in Chapter 2, BiOCl_{75%}/BiOBr_{25%} composites exhibited the highest photocatalytic activity. Therefore, it was further used for the preparation of ternary system using three different rGO ratios. Calculated band gap energy of the prepared ternary system using Tauc plot method is depicted in Figure 15. As presented in the figure BiOCl_{75%}/BiOBr_{25%} composite and the ternary system of 1%rGO and 3%rGO show almost same calculated band gap energies of 3.1 eV. However, system containing 5%rGO showed a bit lower band gap energy value of 3.02 eV (Table 5).

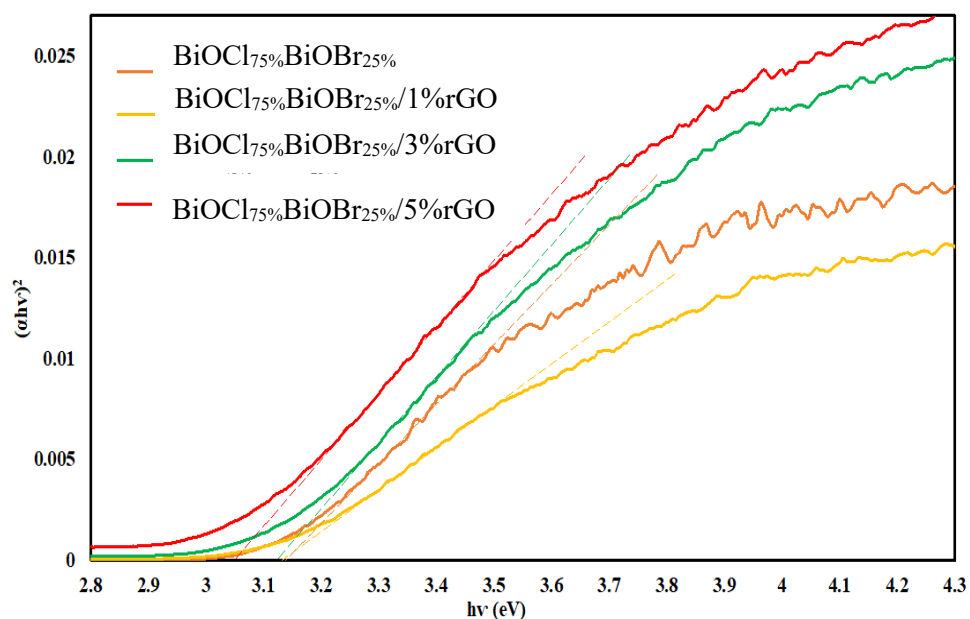


Figure 15: Tauc plot for the prepared BiOCl_{75%}BiOBr_{25%} and BiOCl_{75%}BiOBr_{25%}/rGO composites

Table 4: Lattice parameters for BiOCl_{75%}/BiOBr_{25%} and BiOCl_{75%}/BiOBr_{25%}/rGO composites

Sample	Lattice parameters				
		a=b	c	V Å ³	α=β=γ
BiOCl _{75%} BiOBr _{25%}	BiOCl	3.91	7.53	110.69	90
	BiOBr	3.94	8.32	129.53	
BiOCl _{75%} BiOBr _{25%} /1%rGO	BiOCl	4.38	8.54	163.91	90
	BiOBr	4.30	9.42	174.04	
BiOCl _{75%} BiOBr _{25%} /3%rGO	BiOCl	4.36	8.47	160.70	90
	BiOBr	4.32	9.33	174.58	
BiOCl _{75%} BiOBr _{25%} /5%rGO	BiOCl	4.35	8.44	159.88	90
	BiOBr	4.29	9.33	171.97	

Table 5: Physical properties of BiOCl_{75%}/BiOBr_{25%} and BiOCl_{75%}/BiOBr_{25%}/rGO composites

Samples	Pore size (nm)	Surface area (m ² /g)	Band gap (eV)
BiOCl _{75%} BiOBr _{25%}	102.57	3.98	3.13
BiOCl _{75%} BiOBr _{25%} /1%rGO	115.16	5.23	3.11
BiOCl _{75%} BiOBr _{25%} /3%rGO	101.27	4.22	3.00
BiOCl _{75%} BiOBr _{25%} /5%rGO	112.02	4.68	2.99

3.5.3 BET Surface Analysis for BiOCl_{75%}/BiOBr_{25%}/rGO Composites

Figure 16 demonstrate N₂ adsorption-desorption analysis of BiOCl_{75%}/BiOBr_{25%} and BiOCl_{75%}BiOBr_{25%}/rGO ternary composites. Brunnauer-Emmett-Teller (BET) was used to calculate the surface area of the prepared samples which found to be 5.2270 m²/g, 4.2235 m²/g, 4.6756 m²/g, for 1% rGO, 3% rGO and 5% rGO respectively. The prepared samples exhibited type III isotherm with a hysteresis loop observed between 0.7-1.0 P/P₀. All calculated data are reported in Table 5.

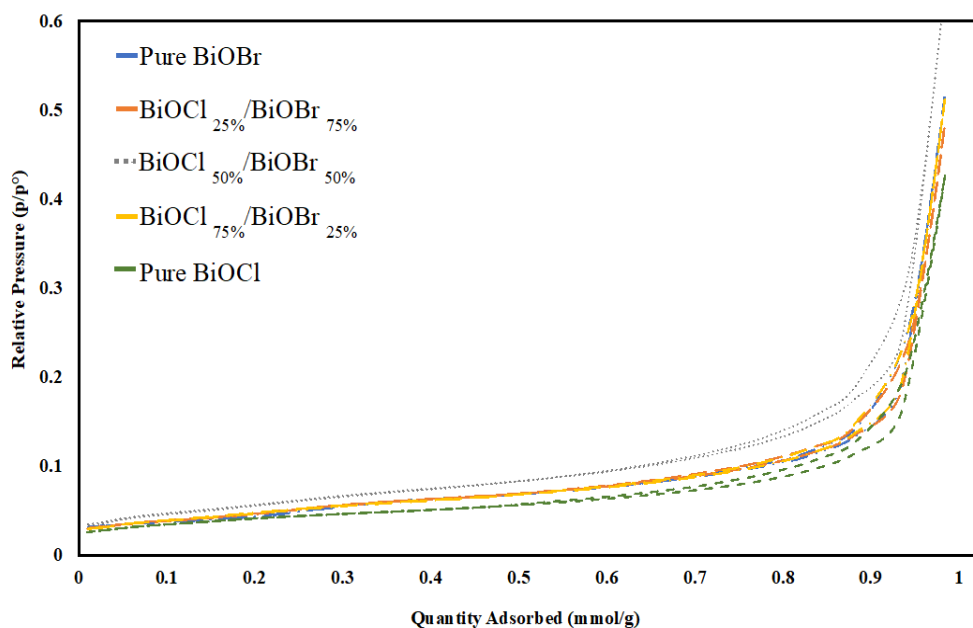


Figure 16: BET analysis for the prepared BiOCl_{75%}/BiOBr_{25%} and BiOCl_{75%}BiOBr_{25%}/rGO ternary composites

3.5.4 Morphology Characterization (SEM) and Elemental Analysis (EDX)

SEM images of the prepared rGO composites are presented in Figure 17, as percent rGO increases in the composites no change in morphology was observed, where different composites show the same agglomerated particles, indicating that rGO has no effect on the morphology due to the low rGO content added to the photocatalyst.

EDX analysis was used to confirm the elemental composition of the prepared composites. Figure 18 confirms the existence of Bi, O, Cl, Br and C with no extra peaks of any impurities. As shown in Table 6 and Table 7, the high percentage of C the composites show can be explained by the use carbon tape in the analysis process.

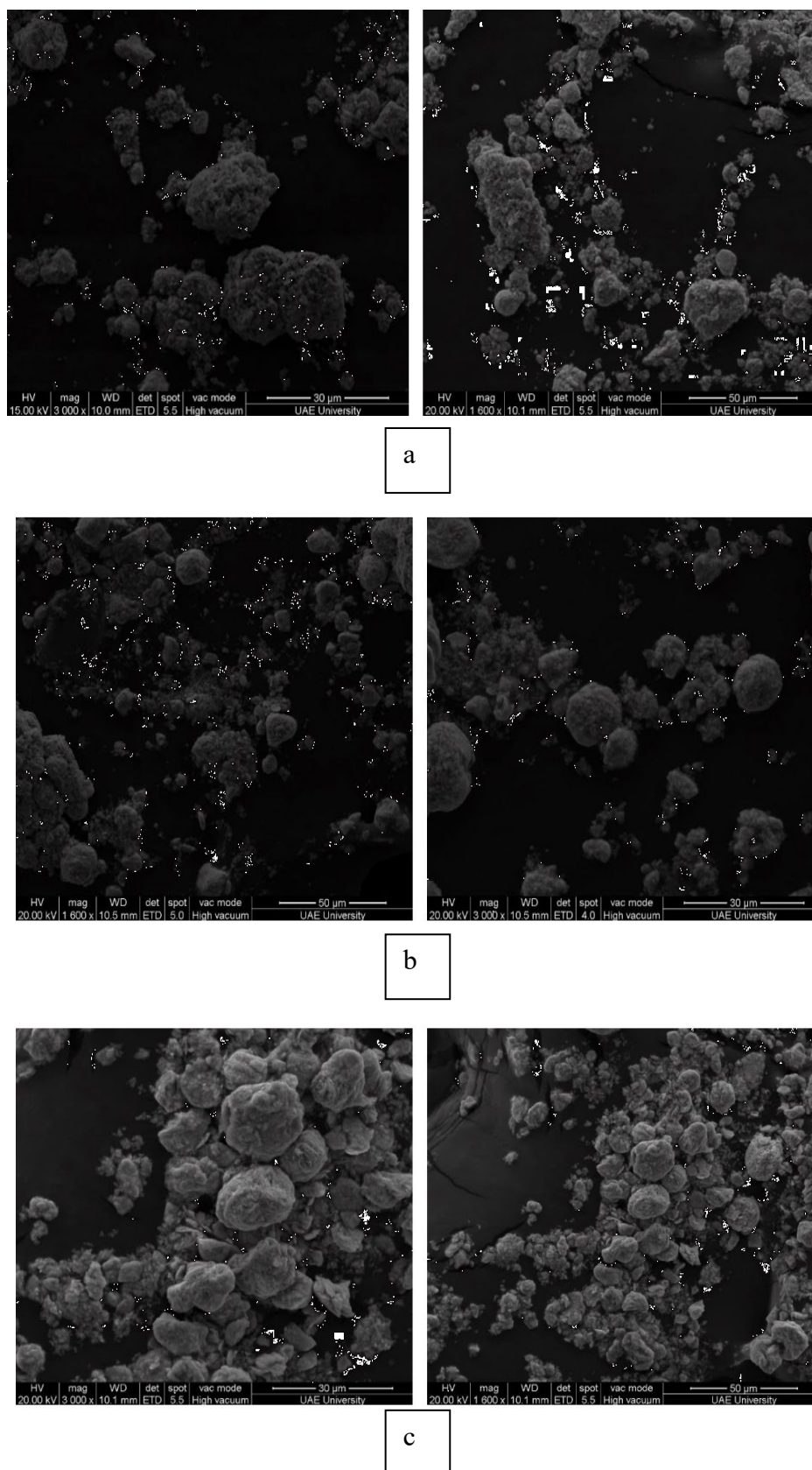


Figure 17: SEM images for (a) BiOCl_{75%}BiOBr_{25%}/1%rGO (b) BiOCl_{75%}BiOBr_{25%}/3%rGO and (c) BiOCl_{75%}BiOBr_{25%}/5%rGO

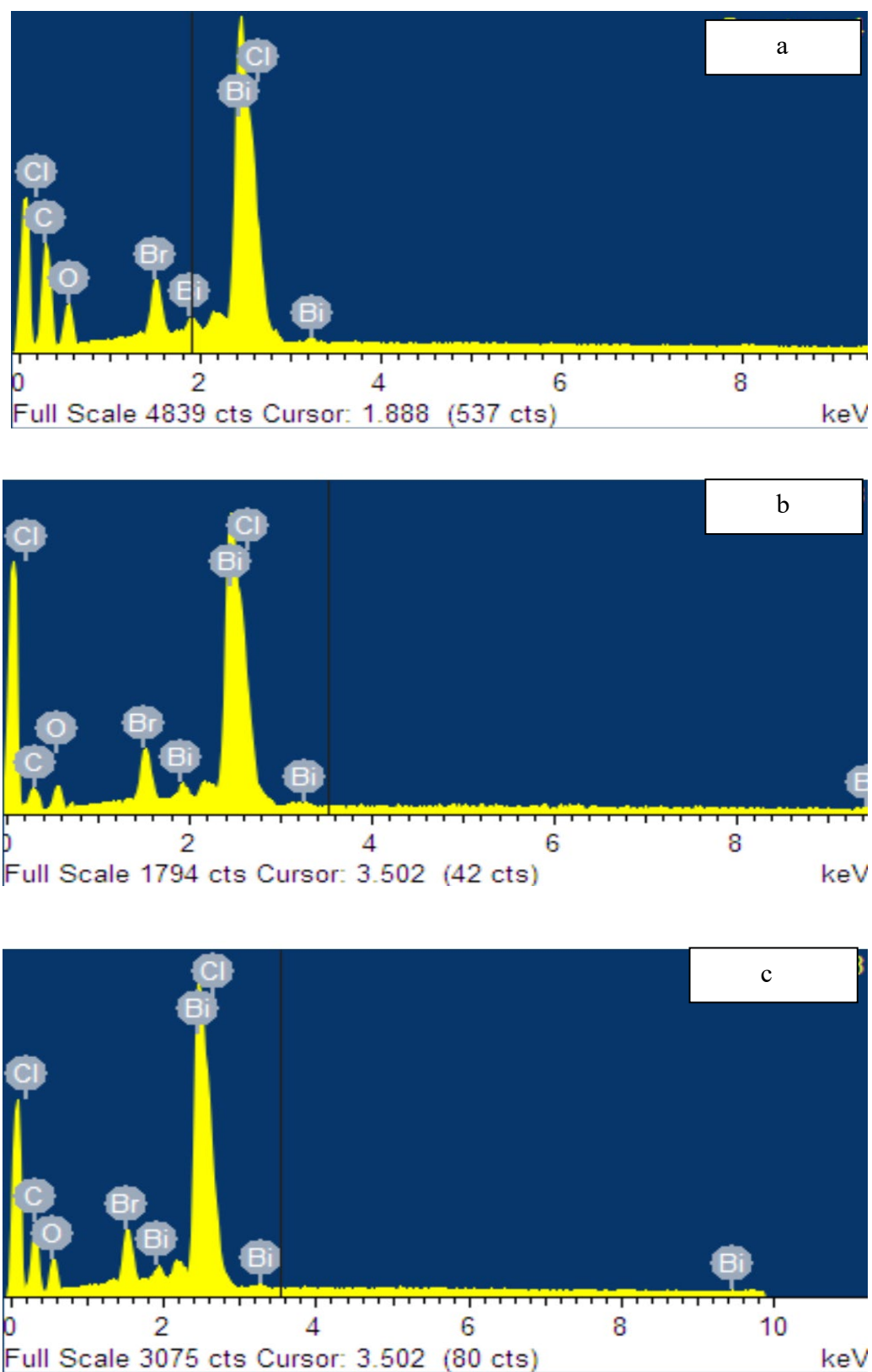


Figure 18: EDX of BiOCl_{75%}BiOBr_{25%}/rGO ternary composites (a) BiOCl_{75%}BiOBr_{25%}/1%rGO (b) BiOCl_{75%}BiOBr_{25%}/3%rGO and (c) BiOCl_{75%}BiOBr_{25%}/5%rGO

Table 6: Atomic percentage of BiOCl_{75%}BiOBr_{25%}/rGO composites

Samples	Atomic %				
	O	Bi	Cl	Br	C
BiOCl _{75%} BiOBr _{25%}	46.79	29.01	16.45	7.75	-
BiOCl _{75%} BiOBr _{25%} / 1rGO	21.75	6.05	3.55	1.49	67.15
BiOCl _{75%} BiOBr _{25%} / 3rGO	28.75	13.86	8.04	3.62	45.73
BiOCl _{75%} BiOBr _{25%} / 5rGO	22.97	8.35	4.68	2.08	61.92

Table 7: Weight percentage of BiOCl_{75%}BiOBr_{25%}/rGO composites

Samples	Weight %				
	O	Bi	Cl	Br	C
BiOCl _{75%} BiOBr _{25%}	9.34	75.66	7.28	7.73	-
BiOCl _{75%} BiOBr _{25%} / 1rGO	13.06	47.48	4.73	4.46	30.27
BiOCl _{75%} BiOBr _{25%} / 3rGO	10.27	64.65	6.37	6.46	12.26
BiOCl _{75%} BiOBr _{25%} / 5rGO	11.53	54.72	5.20	5.22	23.33

3.5.5 Photocatalytic Activity of the BiOCl_{75%}/BiOBr_{25%} Composite and BiOCl_{75%}BiOBr_{25%}/ rGO Ternary Composites

Figure 19 display the photoreduction of 4-NA to PPD using the different rGO ratio composites BiOCl_{75%}BiOBr_{25%}/rGO under visible light irradiation as a function

of time. Reaction was monitored by observing the decrease in absorption at $\lambda = 380$ nm that corresponds to the reduction of 4-NA. Moreover, the appearance of two new peaks at 283 nm and 305 nm as irradiation time increases corresponds to the formation of PPD. As reported in Table 8, the reaction rate constant increases as the rGO load increase in the sample. BiOCl_{75%}BiOBr_{25%}/5%rGO composite showed the highest rate constant of 0.84 min⁻¹ that can be ascribed to the role of rGO in trapping electrons by acting as a sheet, hence minimizing the recombination rate. Lowering the recombination rate provides more electrons in the conduction band to produce OH radicals for the reduction of 4-NA as discussed earlier in Chapter 2 Figure 12. An attempt to evaluate the photocatalytic performance at higher rGO loading 10% resulted in a drop in the photocatalytic performance which may be attributed to the more light absorption of rGO at higher load. All prepared composites exhibited excellent conversion percentage more than 98%. TiO₂ exhibited the lowest rate constant of 0.028 min⁻¹ compared to the prepared visible light active composites. Moreover, the use of NaBH₄ presented a low-rate constant emphasizing the role of the photocatalyst for the reaction to complete. C/C_0 vs. time graph demonstrate the change in concentration of 4-NA under visible light irradiation using various photocatalysts for 20 min Figure 20. A reaction follows first order kinetics where obtained experimental data shows straight line for chosen concentration range Figure 21. $\ln(C/C_0)$ graph as a variation of time is presented in Figure 21. Moreover, calculated rate constant for the prepared samples is demonstrated in Figure 22. As discussed, two mechanisms were suggested for photoreduction of 4-NA to PPD in aqueous solution. Reaction can proceed through the hydroxyl radical generated by the excited e⁻ over the conduction band or generated holes in the valence band.

Table 8: Photocatalytic kinetics data for the reduction of 4-NA to PPD

Photocatalyst	K (min ⁻¹)	Conversion (%) after 20 min
BiOCl _{75%} BiOBr _{25%}	0.29	99.4
BiOCl _{75%} BiOBr _{25%} /1%rGO	0.59	100
BiOCl _{75%} BiOBr _{25%} /3%rGO	0.82	99.17
BiOCl _{75%} BiOBr _{25%} /5%rGO	0.84	98.80
NaBH ₄ without photocatalyst	0.038	41.3
TiO ₂	0.028	17.6

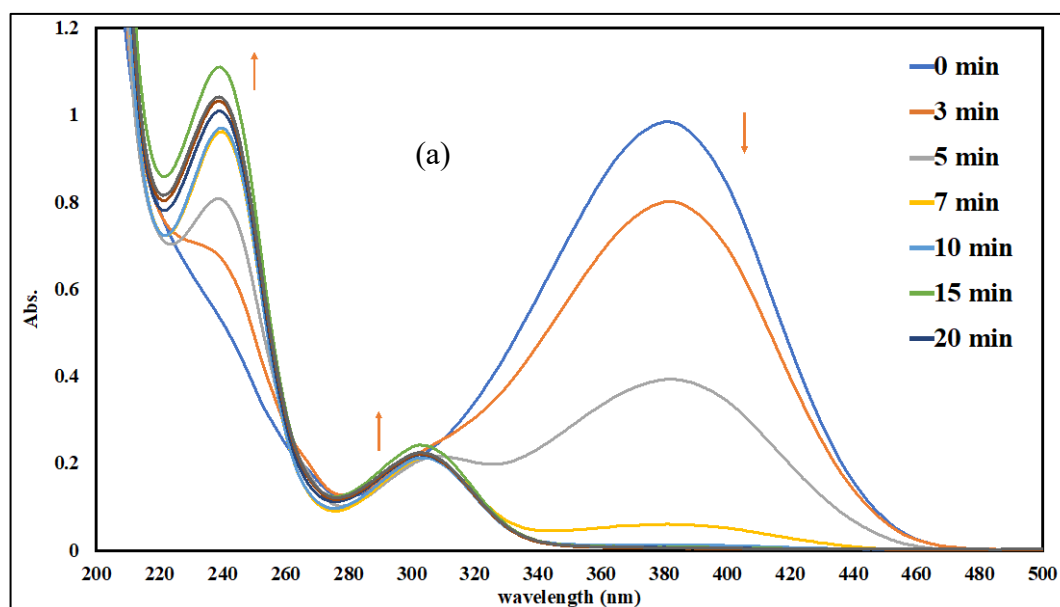


Figure 19: Concentration variation of 4-NA over time under visible light irradiation in the presence of (a) BiOCl_{75%}BiOBr_{25%} (b) BiOCl_{75%}BiOBr_{25%}/1%rGO (c) BiOCl_{75%}BiOBr_{25%}/3%rGO (d) BiOCl_{75%}BiOBr_{25%}/5%rGO (e) NaBH₄ and (f) TiO₂ photocatalysts

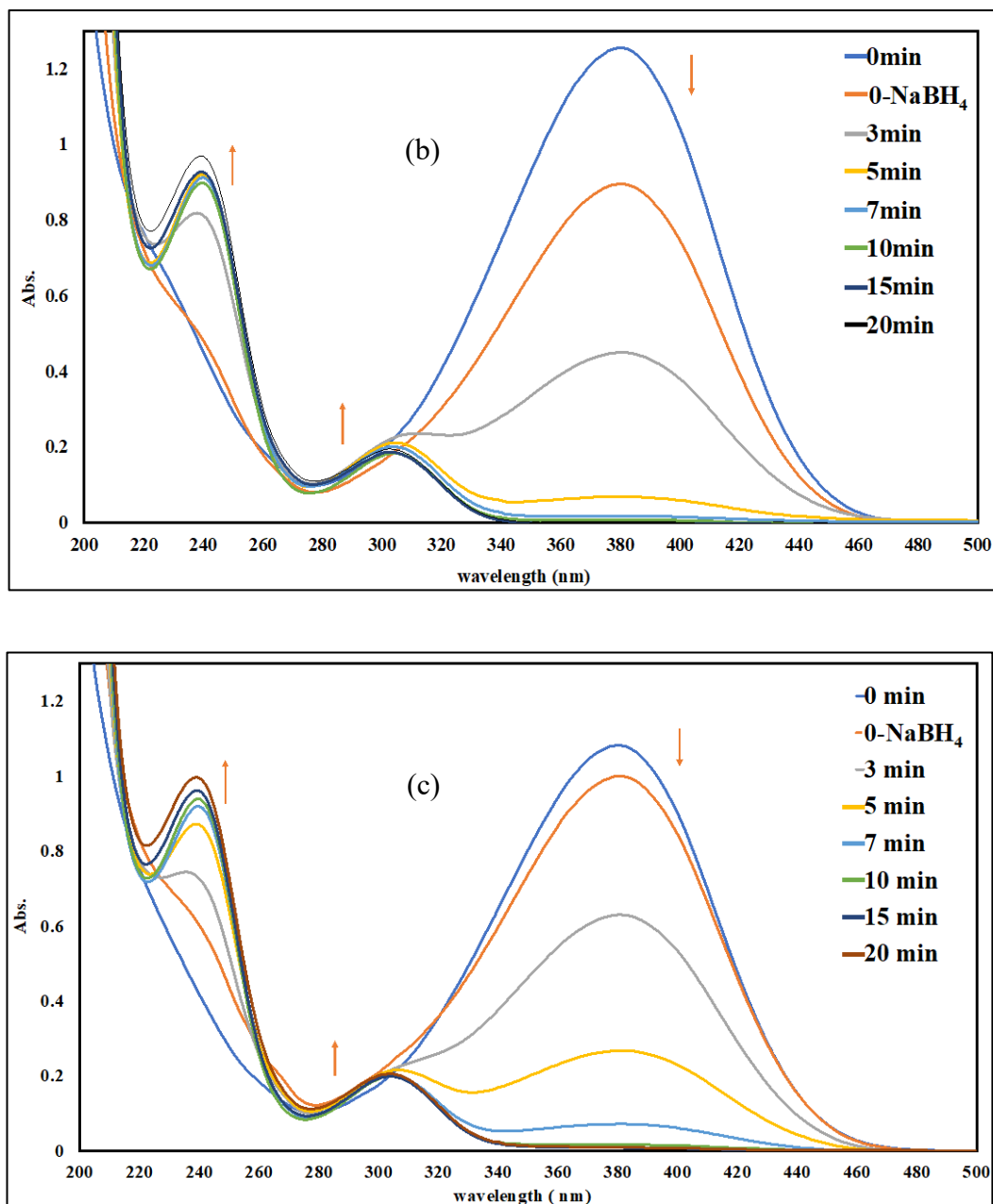


Figure 19: Concentration variation of 4-NA over time under visible light irradiation in the presence of (a) $\text{BiOCl}_{75\%}\text{BiOBr}_{25\%}$ (b) $\text{BiOCl}_{75\%}\text{BiOBr}_{25\%}/1\%\text{rGO}$ (c) $\text{BiOCl}_{75\%}\text{BiOBr}_{25\%}/3\%\text{rGO}$ (d) $\text{BiOCl}_{75\%}\text{BiOBr}_{25\%}/5\%\text{rGO}$ (e) NaBH_4 and (f) TiO_2 photocatalysts (continued)

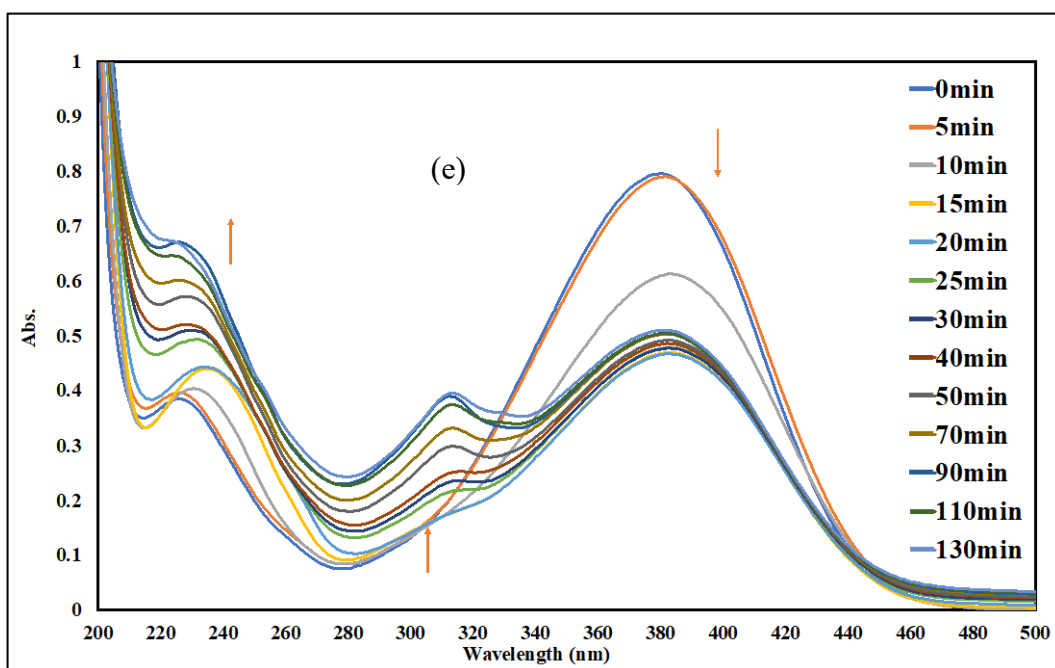
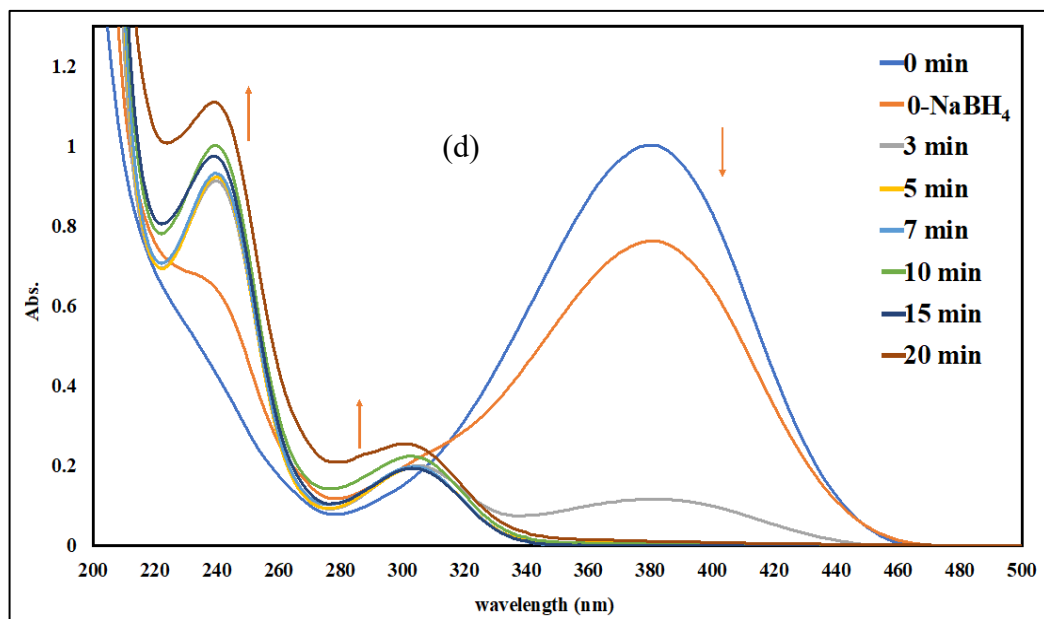


Figure 19: Concentration variation of 4-NA over time under visible light irradiation in the presence of (a) $\text{BiOCl}_{75\%}\text{BiOBr}_{25\%}$ (b) $\text{BiOCl}_{75\%}\text{BiOBr}_{25\%}/1\%\text{rGO}$ (c) $\text{BiOCl}_{75\%}\text{BiOBr}_{25\%}/3\%\text{rGO}$ (d) $\text{BiOCl}_{75\%}\text{BiOBr}_{25\%}/5\%\text{rGO}$ (e) NaBH_4 and (f) TiO_2 photocatalysts (continued)

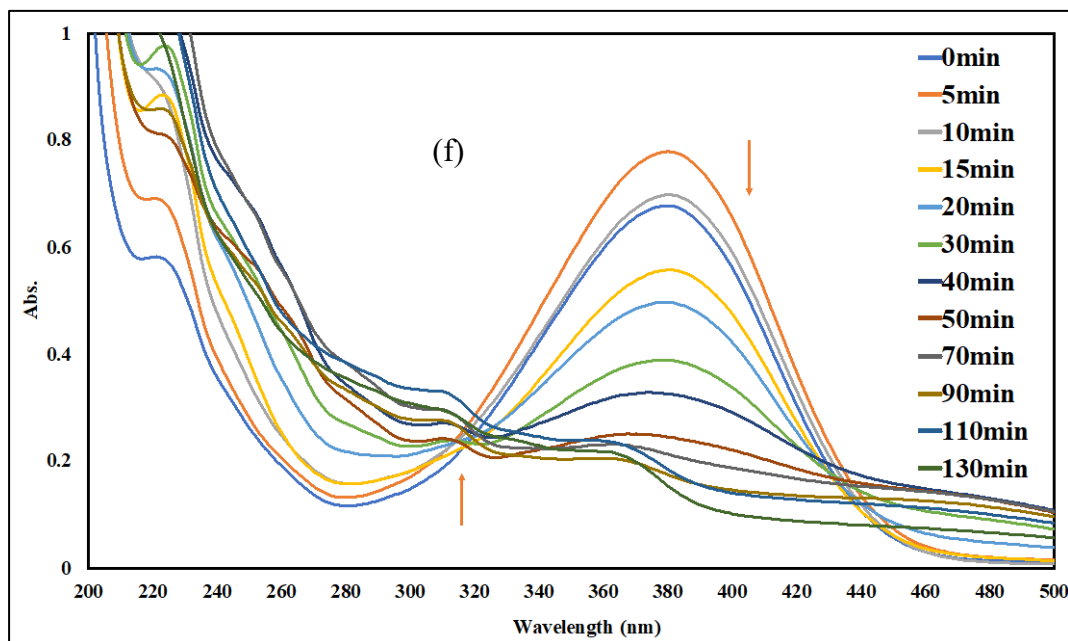


Figure 19: Concentration variation of 4-NA over time under visible light irradiation in the presence of (a) $\text{BiOCl}_{75\%}\text{BiOBr}_{25\%}$ (b) $\text{BiOCl}_{75\%}\text{BiOBr}_{25\%}/1\%\text{rGO}$ (c) $\text{BiOCl}_{75\%}\text{BiOBr}_{25\%}/3\%\text{rGO}$ (d) $\text{BiOCl}_{75\%}\text{BiOBr}_{25\%}/5\%\text{rGO}$ (e) NaBH_4 and (f) TiO_2 photocatalysts (continued)

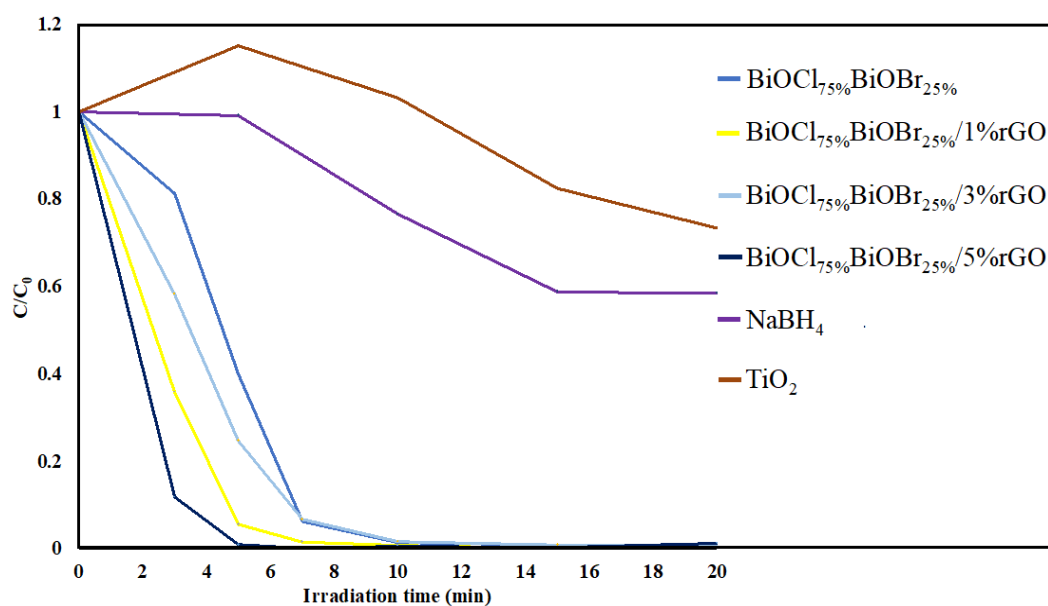


Figure 20: Concentration variation of 4-nitroaniline over time using $\text{BiOCl}_{75\%}\text{BiOBr}_{25\%}$, $\text{BiOCl}/\text{BiOBr}/\text{rGO}$ composites, NaBH_4 and TiO_2 photocatalysts under visible light irradiation

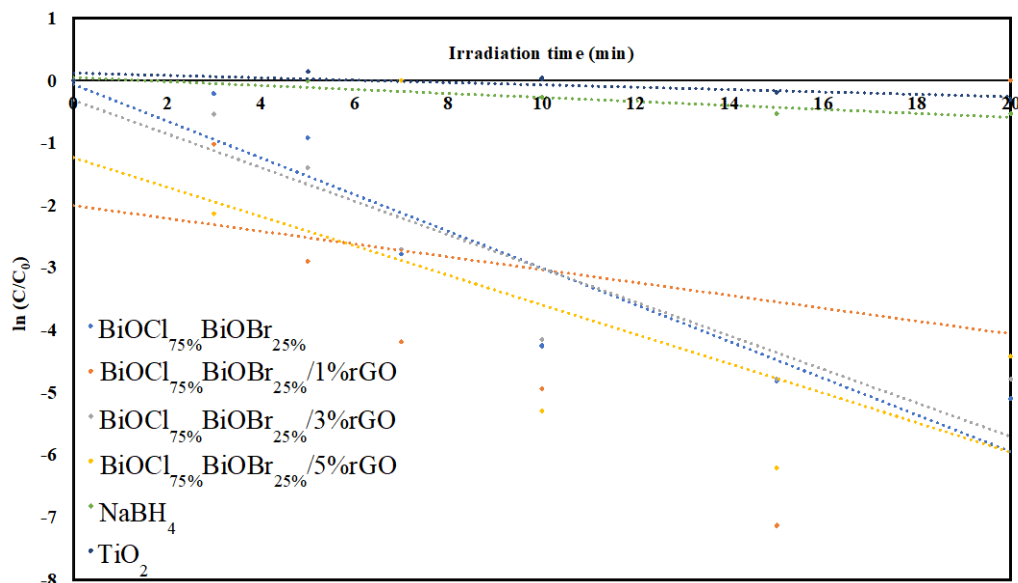


Figure 21: Kinetics plot of $\ln C/C_0$ over time of $\text{BiOCl}_{75\%}\text{BiOBr}_{25\%}$, $\text{BiOCl}/\text{BiOBr}/\text{rGO}$ composites, NaBH_4 and TiO_2 photocatalysts

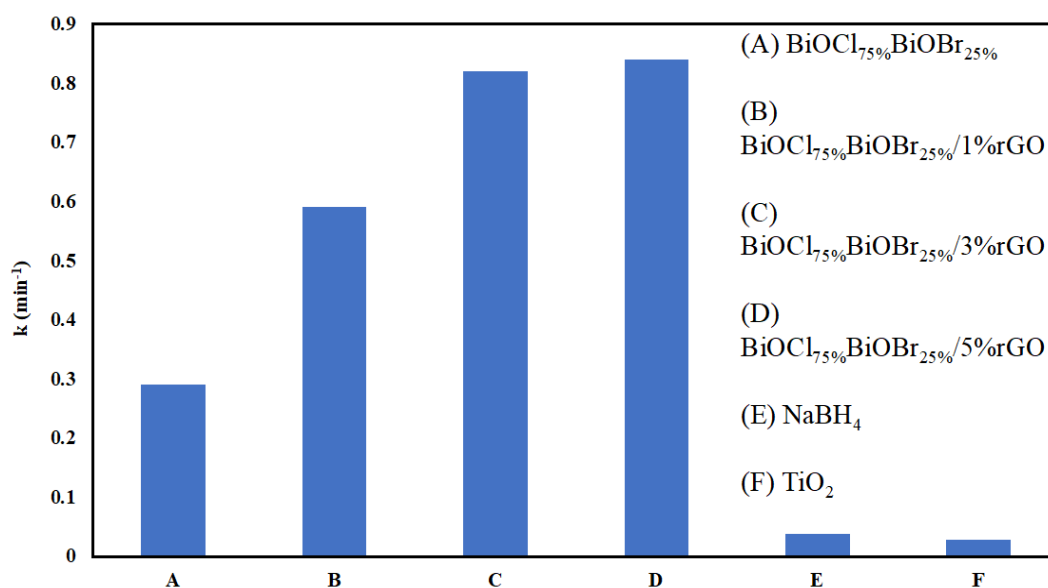


Figure 22: Calculated rate constants for $\text{BiOCl}_{75\%}\text{BiOBr}_{25\%}$, $\text{BiOCl}/\text{BiOBr}/\text{rGO}$ composites, NaBH_4 and TiO_2

3.6 Conclusion

In conclusion, XRD diffraction pattern confirms the successful incorporation of different rGO ratios into $\text{BiOCl}_{75\%}/\text{BiOBr}_{25\%}$ composite. Characterization showed that

upon the increase of rGO load no change was observed for calculated band gap and morphology for the prepared photocatalysts. BiOCl_{75%}/BiOBr_{25%}/1%rGO exhibited higher surface compared to BiOCl_{75%}/BiOBr_{25%} composite and the two BiOCl_{75%}/BiOBr_{25%}/3%rGO and BiOCl_{75%}/BiOBr_{25%}/5%rGO composites. The photocatalytic activity was evaluated for the photoreduction of 4-NA, results show that as percent rGO increased rate constant increased. Where composite of 5%rGO load has the highest photocatalytic activity and the additional reaction of 10%rGO loading conclude that 5% rGO is the optimum mass ratio for the developed system.

Chapter 4: Conclusion and Future Work

4.1 Conclusion

Pure BiOCl and BiOBr were successfully synthesized using the coprecipitation method. In addition, three different molar ratio composites were synthesized through simple mechanical mixing. The obtained results confirm the purity of the prepared photocatalysts. Calculated band gap value for the different mole ratio composites was almost the same, where varying the mole ratio of BiOCl and BiOBr in the composites showed no change in band gap value. Pure BiOCl and BiOBr presented flake-like morphology, however, the different composites displayed agglomerated particles. The photocatalytic activity of the prepared samples was evaluated toward the photoreduction of 4-NA to PPD. Prepared composites showed higher photocatalytic activity compared to pure BiOCl under visible light irradiation.

BiOCl_{75%}/BiOBr_{25%} composite exhibited the highest photocatalytic activity, so it was further synthesized incorporating rGO. Three different rGO mass ratio composites were prepared and characterized. XRD pattern confirms the existence of rGO in the samples. Results revealed that rGO has almost no effect on band gap and morphology, which can be ascribed to the low rGO amount added to the composites. BiOCl_{75%}/BiOBr_{25%}/5%rGO was found to be the optimum mass ratio to be added, where it exhibited the highest photocatalytic activity. Reduced graphene oxide acts as electron trap preventing the recombination of electron/hole pairs therefore it enhances the performance of the photocatalyst. The photoreduction of 4-NA to PPD can proceed through two possible mechanisms. Through the production of OH radicals in the

conduction band and through the reduction by electron holes available on the photocatalysts active sites.

4.2 Further Studies

In the future, the efficiency of the prepared photocatalysts will be evaluated toward different nitroaromatic compounds. Furthermore, other synthetic methods could be implemented to study their effect on the photocatalytic performance of the catalysts. In addition, ^{13}C NMR could be implemented to understand formed chemical species throughout the reaction and provide a full understanding on reaction mechanism.

References

- [1] F. Lu and D. Astruc, "Nanomaterials for removal of toxic elements from water," *Coord. Chem. Rev.*, vol. 356, pp. 147–164, 2018.
- [2] M. F. R. Samsudin, S. Sufian, and B. H. Hameed, "Epigrammatic progress and perspective on the photocatalytic properties of BiVO₄-based photocatalyst in photocatalytic water treatment technology: A review," *J. Mol. Liq.*, vol. 268, pp. 438–459, 2018.
- [3] C. Bi, J. Cao, H. Lin, Y. Wang, and S. Chen, "Tunable photocatalytic and photoelectric properties of I⁻-doped BiOBr photocatalyst: dramatic pH effect," *RSC Adv.*, vol. 6, no. 19, pp. 15525–15534, 2016.
- [4] M. Nasr, C. Eid, R. Habchi, P. Miele, and M. Bechelany, "Recent progress on titanium dioxide nanomaterials for Photocatalytic applications," *ChemSusChem*, vol. 11, no. 18, pp. 3023–3047, 2018.
- [5] R. B. Arthur, J. C. Ahern, and H. H. Patterson, "Application of BiOX photocatalysts in remediation of persistent organic pollutants," *Catalysts*, vol. 8, no. 12, pp. 604–629, 2018.
- [6] Y. Choi *et al.*, "TiO₂/BiOX (X = Cl, Br, I) hybrid microspheres for artificial waste water and real sample treatment under visible light irradiation," *Sep. Purif. Technol.*, vol. 160, pp. 28–42, 2016.
- [7] I. K. Konstantinou and T. A. Albanis, "TiO₂-assisted photocatalytic degradation of azo dyes in aqueous solution: kinetic and mechanistic investigations: A review," *Appl. Catal. B Environ.*, vol. 49, no. 1, pp. 1–14, 2004.
- [8] Y. Su *et al.*, "First hydrothermal synthesis of Bi₅O₇Br and its photocatalytic properties for molecular oxygen activation and RhB degradation," *Appl. Surf. Sci.*, vol. 346, pp. 311–316, 2015.
- [9] D. S. Bhachu *et al.*, "Bismuth oxyhalides: synthesis, structure and photoelectrochemical activity," *Chem. Sci.*, vol. 7, no. 8, pp. 4832–4841, 2016.
- [10] M. Jia, X. Hu, S. Wang, Y. Huang, and L. Song, "Photocatalytic properties of hierarchical BiOXs obtained via an ethanol-assisted solvothermal process," *J. Environ. Sci.*, vol. 35, pp. 172–180, 2015.
- [11] S. P. Adhikari and A. Lachgar, "Effect of particle size on the photocatalytic activity of BiNbO₄ under visible light irradiation," *J. Phys. Conf. Ser.*, vol. 758, p. 12017, 2016.
- [12] A. Henríquez, H. D. Mansilla, A. M. Martínez-de la Cruz, J. Freer, and D. Contreras, "Selective oxofunctionalization of cyclohexane over titanium dioxide-based and bismuth oxyhalide (BiOX, X= Cl⁻, Br⁻, I⁻) photocatalysts by visible light irradiation," *Appl. Catal. B Environ.*, vol. 206, pp. 252–262, 2017.

- [13] J. C. Ahern, R. Fairchild, J. S. Thomas, J. Carr, and H. H. Patterson, "Characterization of BiOX compounds as photocatalysts for the degradation of pharmaceuticals in water," *Appl. Catal. B Environ.*, vol. 179, pp. 229–238, 2015.
- [14] X. Zhang, G. Xu, J. Hu, J. Lv, J. Wang, and Y. Wu, "Fabrication and photocatalytic performances of BiOCl nanosheets modified with ultrafine Bi₂O₃ nanocrystals," *RSC Adv.*, vol. 6, no. 68, pp. 63241–63249, 2016.
- [15] B. O. Bica and J. V. S. de Melo, "Concrete blocks nano-modified with zinc oxide (ZnO) for photocatalytic paving: performance comparison with titanium dioxide (TiO₂)," *Constr. Build. Mater.*, vol. 252, pp. 119120–119132, 2020.
- [16] E. Leyva, C. Montalvo, E. Moctezuma, and S. Leyva, "Photocatalytic degradation of pyridine in water solution using ZnO as an alternative catalyst to TiO₂," *J. Ceram. Process. Res.*, vol. 9, pp. 455–462, 2008.
- [17] R. Fiorenza *et al.*, "CeO₂ for Water Remediation: Comparison of Various Advanced Oxidation Processes," *Catalysts*, vol. 10, no. 4, pp. 446–462, 2020.
- [18] R. He, D. Xu, B. Cheng, J. Yu, and W. Ho, "Review on nanoscale Bi-based photocatalysts," *Nanoscale Horizons*, vol. 3, no. 5, pp. 464–504, 2018.
- [19] M. D. Hernández-Alonso, F. Fresno, S. Suárez, and J. M. Coronado, "Development of alternative photocatalysts to TiO₂: challenges and opportunities," *Energy Environ. Sci.*, vol. 2, no. 12, pp. 1231–1257, 2009.
- [20] S. Wang, D. Li, C. Sun, S. Yang, Y. Guan, and H. He, "Synthesis and characterization of g-C₃N₄/Ag₃VO₄ composites with significantly enhanced visible-light photocatalytic activity for triphenylmethane dye degradation," *Appl. Catal. B Environ.*, vol. 144, pp. 885–892, 2014.
- [21] X. Hu and C. Hu, "Preparation and visible-light photocatalytic activity of Ag₃VO₄ powders," *J. Solid State Chem.*, vol. 180, no. 2, pp. 725–732, 2007.
- [22] T. Saison *et al.*, "Bi₂O₃, BiVO₄, and Bi₂WO₆: Impact of surface properties on photocatalytic activity under visible light," *J. Phys. Chem. C*, vol. 115, no. 13, pp. 5657–5666, 2011.
- [23] X. Jin, L. Ye, H. Xie, and G. Chen, "Bismuth-rich bismuth oxyhalides for environmental and energy photocatalysis," *Coord. Chem. Rev.*, vol. 349, pp. 84–101, 2017.
- [24] J. Li *et al.*, "Uniform flower-like BiOBr/BiOI prepared by a new method: visible-light photocatalytic degradation, influencing factors and degradation mechanism," *New J. Chem.*, vol. 43, pp. 14829–14840, 2019.
- [25] S. Xue *et al.*, "Enhanced visible-light photocatalytic activities and mechanism insight of BiVO₄/Bi₂WO₆ composites with virus-like structures," *Appl. Surf. Sci.*, vol. 355, pp. 1107–1115, 2015.

- [26] J. Xiong, P. Song, J. Di, H. Li, and Z. Liu, "Freestanding ultrathin bismuth-based materials for diversified photocatalytic applications," *J. Mater. Chem. A*, vol. 7, no. 44, pp. 25203–25226, 2019.
- [27] A. Han, H. Zhang, G.-K. Chuah, and S. Jaenicke, "Influence of the halide and exposed facets on the visible-light photoactivity of bismuth oxyhalides for selective aerobic oxidation of primary amines," *Appl. Catal. B Environ.*, vol. 219, pp. 269–275, 2017.
- [28] G. Zhang, Y. Tan, Z. Sun, and S. Zheng, "Synthesis of BiOCl/TiO₂ heterostructure composites and their enhanced photocatalytic activity," *J. Environ. Chem. Eng.*, vol. 5, pp. 1196–1204, 2017.
- [29] H. Zhang, L. Liu, and Z. Zhou, "First-principles studies on facet-dependent photocatalytic properties of bismuth oxyhalides (BiOXs)," *RSC Adv.*, vol. 2, no. 24, pp. 9224–9229, 2012.
- [30] J. Zhao, X. Lv, X. Wang, J. Yang, X. Yang, and X. Lu, "Fabrication of BiOX (X=Cl, Br, and I) nanosheeted films by anodization and their photocatalytic properties," *Mater. Lett.*, vol. 158, pp. 40–44, 2015.
- [31] Z. Wang *et al.*, "Multiply structural optimized strategies for bismuth oxyhalide photocatalysis and their environmental application," *Chem. Eng. J.*, vol. 374, pp. 1025–1045, 2019.
- [32] A. Bielicka-Giełdoń *et al.*, "Morphology, surface properties and photocatalytic activity of the bismuth oxyhalides semiconductors prepared by ionic liquid assisted solvothermal method," *Sep. Purif. Technol.*, vol. 217, pp. 164–173, 2019.
- [33] K. Sharma *et al.*, "Recent advances in enhanced photocatalytic activity of bismuth oxyhalides for efficient photocatalysis of organic pollutants in water: A review," *J. Ind. Eng. Chem.*, vol. 78, pp. 1–20, 2019.
- [34] S. Garg, M. Yadav, A. Chandra, and K. Hernadi, "A review on BiOX (X= Cl, Br and I) nano-/microstructures for their photocatalytic applications," *J. Nanosci. Nanotechnol.*, vol. 19, no. 1, pp. 280–294, 2019.
- [35] L. S. Gómez-Velázquez, A. Hernández-Gordillo, M. J. Robinson, V. J. Leppert, S. E. Rodil, and M. Bizarro, "The bismuth oxyhalide family: thin film synthesis and periodic properties," *Dalt. Trans.*, vol. 47, no. 35, pp. 12459–12467, 2018.
- [36] J. Wu *et al.*, "Synthesis of flower-like g-C₃N₄/BiOBr and enhancement of the activity for the degradation of bisphenol A under visible light irradiation," *Front. Chem.*, vol. 7, pp. 649–661, 2019.
- [37] A. M. Ganose, M. Cuff, K. T. Butler, A. Walsh, and D. O. Scanlon, "Interplay of orbital and relativistic effects in bismuth oxyhalides: BiOF, BiOCl, BiOBr, and BiOI," *Chem. Mater.*, vol. 28, no. 7, pp. 1980–1984, 2016.
- [38] S. Dutta, T. Das, and S. Datta, "Impact of bi-axial strain on the structural, electronic and optical properties of photo-catalytic bulk bismuth oxyhalides," *Phys. Chem. Chem. Phys.*, vol. 20, no. 1, pp. 103–111, 2018.

- [39] K. Ren *et al.*, “Synthesis of the bismuth oxyhalide solid solutions with tunable band gap and photocatalytic activities,” *Dalt. Trans.*, vol. 42, no. 26, pp. 9706–9712, 2013.
- [40] G. Tripathi and R. Kurchania, “Photocatalytic behavior of BiOX (X = Cl/Br, Cl/I and Br/I) composites/heterogeneous nanostructures with organic dye,” *Opt. Quantum Electron.*, vol. 49, pp. 203–220, 2017.
- [41] B. Zhang *et al.*, “Rapid adsorption properties of flower-like BiOI nanoplates synthesized via a simple EG-assisted solvothermal process,” *J. nanoparticle Res.*, vol. 15, no. 7, pp. 1773–1782, 2013.
- [42] J. Wu and X. Cao, “Growth of bismuth oxyhalide nanoplates on self-standing TiO₂ nanowire film exhibiting enhanced photoelectrochemical performances,” *Electrochim. Acta*, vol. 247, pp. 646–656, 2017.
- [43] Y. Gu *et al.*, “Preparation and characterization of highly photocatalytic active hierarchical BiOX (X=Cl, Br, I) microflowers for rhodamine B degradation with kinetic modelling studies,” *J. Cent. South Univ.*, vol. 24, pp. 754–765, 2016.
- [44] C. Ding *et al.*, “Large-scale preparation of BiOX (X = Cl, Br) ultrathin nanosheets for efficient photocatalytic CO₂ conversion,” *J. Taiwan Inst. Chem. Eng.*, vol. 78, pp. 395–400, 2017.
- [45] H. Li, J. Liu, T. Hu, N. Du, S. Song, and W. Hou, “Synthesis of belt-like BiOBr hierarchical nanostructure with high photocatalytic performance,” *Mater. Res. Bull.*, vol. 77, pp. 171–177, 2016.
- [46] W. Zhang and Y. Liang, “Facile synthesis of ternary g-C₃N₄@BiOCl/Bi₁₂O₁₇C₁₂ composites with excellent visible light photocatalytic activity for NO removal,” *Frontiers in Chemistry*, vol. 7, pp. 231–241, 2019.
- [47] Y. Ao, K. Wang, P. Wang, C. Wang, and J. Hou, “Synthesis of novel 2D-2D pn heterojunction BiOBr/La₂Ti₂O₇ composite photocatalyst with enhanced photocatalytic performance under both UV and visible light irradiation,” *Appl. Catal. B Environ.*, vol. 194, pp. 157–168, 2016.
- [48] Z. Liu, J. Liu, H. Wang, G. Cao, and J. Niu, “Boron-doped bismuth oxybromide microspheres with enhanced surface hydroxyl groups: synthesis, characterization and dramatic photocatalytic activity,” *J. Colloid Interface Sci.*, vol. 463, pp. 324–331, 2016.
- [49] Z. S. Liu, B. T. Wu, J. N. Niu, P. Z. Feng, and Y. B. Zhu, “BiPO₄/BiOBr p–n junction photocatalysts: one-pot synthesis and dramatic visible light photocatalytic activity,” *Mater. Res. Bull.*, vol. 63, pp. 187–193, 2015.
- [50] X. Zou, H. Fan, Y. Tian, and S. Yan, “Synthesis of Cu₂O/ZnO hetero-nanorod arrays with enhanced visible light-driven photocatalytic activity,” *CrystEngComm*, vol. 16, no. 6, pp. 1149–1156, 2014.

- [51] S. Yin *et al.*, “Ionic liquid-assisted synthesis and improved photocatalytic activity of p-n junction g-C₃N₄/BiOCl,” *J. Mater. Sci.*, vol. 51, pp. 4769–4777, 2016.
- [52] J. Zhang *et al.*, “Improvement of visible light photocatalytic activity over flower-like BiOCl/BiOBr microspheres synthesized by reactable ionic liquids,” *Colloids Surfaces A Physicochem. Eng. Asp.*, vol. 420, pp. 89–95, 2013.
- [53] H. Huang, X. Han, X. Li, S. Wang, P. K. Chu, and Y. Zhang, “Fabrication of multiple heterojunctions with tunable visible-light-active photocatalytic reactivity in BiOBr–BiOI full-range composites based on microstructure modulation and band structures,” *ACS Appl. Mater. Interfaces*, vol. 7, no. 1, pp. 482–492, 2015.
- [54] S. Zhang and J. Yang, “Microwave-assisted synthesis of BiOCl/BiOBr composites with improved visible-light photocatalytic activity,” *Ind. Eng. Chem. Res.*, vol. 54, no. 41, pp. 9913–9919, 2015.
- [55] T. Jiang, J. Li, Y. Gao, L. Li, T. Lu, and L. Pan, “BiOBr/BiOF composites for efficient degradation of rhodamine B and nitrobenzene under visible light irradiation,” *J. Colloid Interface Sci.*, vol. 490, pp. 812–818, 2017.
- [56] J. Xu, G. Tang, W. Liang, D. Zhou, C. Li, and H. Tang, “Surfactant-assisted solvothermal synthesis and high visible-light-induced photocatalytic activity of BiOBr nanocomposite photocatalyst,” *Nano*, vol. 11, no. 01, pp. 1650002–1650008, 2016.
- [57] Y. Liu *et al.*, “Three-dimensional BiOI/BiOX (X= Cl or Br) nanohybrids for enhanced visible-light photocatalytic activity,” *Nanomaterials*, vol. 7, no. 3, pp. 64–83, 2017.
- [58] H. Wang *et al.*, “Highly enhanced visible light photocatalysis and in situ FT-IR studies on Bi metal@defective BiOCl hierarchical microspheres,” *Appl. Catal. B Environ.*, vol. 225, pp. 218–227, 2018.
- [59] S. M. Aghdam, M. Haghghi, S. Allahyari, and L. Yosefi, “Precipitation dispersion of various ratios of BiOI/BiOCl nanocomposite over g-C₃N₄ for promoted visible light nanophotocatalyst used in removal of acid orange 7 from water,” *J. Photochem. Photobiol. A Chem.*, vol. 338, pp. 201–212, 2017.
- [60] Y. Zhong *et al.*, “Facile fabrication of BiOI/BiOCl immobilized films with improved visible light photocatalytic performance,” *Frontiers in Chemistry*, vol. 6, pp. 58–69, 2018.
- [61] Z. Cui, H. Song, S. Ge, W. He, and Y. Liu, “Fabrication of BiOCl/BiOBr hybrid nanosheets with enhanced superoxide radical dominating visible light driven photocatalytic activity,” *Appl. Surf. Sci.*, vol. 467–468, pp. 505–513, 2019.
- [62] L. Wu, Q. Zhang, Z. Li, and X. Liu, “Mechanochemical syntheses of a series of bismuth oxyhalide composites to progressively enhance the visible-light responsive activities for the degradation of bisphenol-A,” *Mater. Sci. Semicond. Process.*, vol. 105, pp. 104733–104741, 2020.

- [63] C. Yang, J. Zhong, J. Li, S. Huang, and R. Duan, "In-situ construction of flower-like BiOBr/BiOCl heterojunctions assembled by thin sheets using an ionic liquid," *Mater. Lett.*, vol. 259, pp. 126766–126770, 2020.
- [64] A. Alzamly *et al.*, "Construction of BiOF/BiOI nanocomposites with tunable band gaps as efficient visible-light photocatalysts," *J. Photochem. Photobiol. A Chem.*, vol. 375, pp. 30–39, 2019.
- [65] H. Razavi-Khosroshahi, S. Mohammadzadeh, M. Hojamberdiev, S. Kitano, M. Yamauchi, and M. Fuji, "BiVO₄/BiOX (X = F, Cl, Br, I) heterojunctions for degrading organic dye under visible light," *Adv. Powder Technol.*, vol. 30, no. 7, pp. 1290–1296, 2019.
- [66] J. Hu, X. Li, X. Wang, Q. Li, and F. Wang, "Novel hierarchical Sn₃O₄/BiOX (X = Cl, Br, I) p–n heterostructures with enhanced photocatalytic activity under simulated solar light irradiation," *Dalt. Trans.*, vol. 48, no. 24, pp. 8937–8947, 2019.
- [67] W. Maisang *et al.*, "Microwave-assisted hydrothermal synthesis of BiOBr/BiOCl flowerlike composites used for photocatalysis," *Res. Chem. Intermed.*, vol. 46, no. 4, pp. 2117–2135, 2020.
- [68] S. Yao, J. Wang, X. Zhou, S. Zhou, X. Pu, and W. Li, "One-pot low-temperature synthesis of BiOX/TiO₂ hierarchical composites of adsorption coupled with photocatalysis for quick degradation of colored and colorless organic pollutants," *Adv. Powder Technol.*, vol. 31, pp. 1924–1932, 2020.
- [69] T. Xu *et al.*, "Ternary BiOBr/TiO₂/Ti₃C₂Tx MXene nanocomposites with heterojunction structure and improved photocatalysis performance," *Chinese Chem. Lett.*, vol. 31, pp. 1022–1025, 2020.
- [70] R. Hassandoost, S. R. Pouran, A. Khataee, Y. Orooji, and S. W. Joo, "Hierarchically structured ternary heterojunctions based on Ce³⁺/Ce⁴⁺ modified Fe₃O₄ nanoparticles anchored onto graphene oxide sheets as magnetic visible-light-active photocatalysts for decontamination of oxytetracycline," *J. Hazard. Mater.*, vol. 376, pp. 200–211, 2019.
- [71] H. Li, M. Zhu, W. Chen, and K. Wang, "Ternary heterojunctions composed of BiOCl, BiVO₄ and nitrogen-doped carbon quantum dots for use in photoelectrochemical sensing: effective charge separation and application to ultrasensitive sensing of dopamine," *Microchim. Acta*, vol. 184, no. 12, pp. 4827–4833, 2017.
- [72] D. Yuan *et al.*, "Synthesis and photocatalytic activity of g-C₃N₄/BiOI/BiOBr ternary composites," *RSC Adv.*, vol. 6, no. 47, pp. 41204–41213, 2016.
- [73] A. Meyer and K. Fischer, "Oxidative transformation processes and products of para-phenylenediamine (PPD) and para-toluenediamine (PTD)—a review," *Environ. Sci. Eur.*, vol. 27, no. 1, pp. 11–27, 2015.

- [74] W. Wu *et al.*, “A simple and highly efficient route for the preparation of p-phenylenediamine by reducing 4-nitroaniline over commercial CdS visible light-driven photocatalyst in water,” *Green Chem.*, vol. 14, no. 6, pp. 1705–1709, 2012.
- [75] H. M. El-Hosainy *et al.*, “Highly selective photocatalytic reduction of o-dinitrobenzene to o-phenylenediamine over non-metal-doped TiO₂ under simulated solar light irradiation,” *Catalysts*, vol. 8, no. 12, pp. 641–653, 2018.
- [76] W. Wu, L. Wen, L. Shen, R. Liang, R. Yuan, and L. Wu, “A new insight into the photocatalytic reduction of 4-nitroaniline to p-phenylenediamine in the presence of alcohols,” *Appl. Catal. B Environ.*, vol. 130–131, pp. 163–167, 2013.
- [77] X.-J. Yang, B. Chen, X.-B. Li, L.-Q. Zheng, L.-Z. Wu, and C.-H. Tung, “Photocatalytic organic transformation by layered double hydroxides: highly efficient and selective oxidation of primary aromatic amines to their imines under ambient aerobic conditions,” *Chem. Commun.*, vol. 50, no. 50, pp. 6664–6667, 2014.
- [78] X. Li, C. Wang, B. Li, Y. Shao, and D. Li, “Efficient light harvesting over a CdS/In₂O₃ photonic crystal photocatalyst for hydrogenation of 4-nitroaniline to p-phenylenediamine,” *Phys. Chem. Chem. Phys.*, vol. 18, no. 40, pp. 27848–27857, 2016.
- [79] W. Wu, R. Lin, L. Shen, R. Liang, R. Yuan, and L. Wu, “Mechanistic insight into the photocatalytic hydrogenation of 4-nitroaniline over band-gap-tunable CdS photocatalysts,” *Phys. Chem. Chem. Phys.*, vol. 15, no. 44, pp. 19422–19426, 2013.
- [80] K. Revathi, S. Palantavida, and B. Kizhakkekilikoodayil Vijayan, “Effective reduction of p-nitroaniline to p-phenylenediamine using Cu-CuO nanocomposite,” *Mater. Today Proc.*, vol. 9, pp. 633–638, 2019.
- [81] J. Xiong *et al.*, “An architecture of CdS/H₂Ti₅O₁₁ ultrathin nanobelt for photocatalytic hydrogenation of 4-nitroaniline with highly efficient performance,” *J. Mater. Chem. A*, vol. 3, no. 13, pp. 6935–6942, 2015.
- [82] Y.-Y. Chai, D.-P. Qu, D.-K. Ma, W. Chen, and S. Huang, “Carbon quantum dots/Zn²⁺ ions doped-CdS nanowires with enhanced photocatalytic activity for reduction of 4-nitroaniline to p-phenylenediamine,” *Appl. Surf. Sci.*, vol. 450, pp. 1–8, 2018.
- [83] A. L. Chibac *et al.*, “Metal-free and heterogeneous photocatalytic reduction of 4-nitroaniline by a poly(ethylene glycol)-supported eosin dye under visible-light exposure,” *ChemCatChem*, vol. 11, no. 14, pp. 3307–3317, 2019.
- [84] R. M. Mohamed and E. S. Aazam, “Photocatalytic conversion of 4-nitroaniline to p-phenylenediamine using Ni/ZnSn(OH)₆ nanoparticles,” *J. Ind. Eng. Chem.*, vol. 20, no. 5, pp. 3329–3334, 2014.

- [85] S. P. Bawane and S. B. Sawant, "Catalytic hydrogenation of p-nitroaniline and 2-methoxy-5-nitroaniline," vol. 10, pp. 627–631, 2003.
- [86] Z. H. Farooqi *et al.*, "Facile synthesis of silver nanoparticles in a crosslinked polymeric system by in situ reduction method for catalytic reduction of 4-nitroaniline," *Environ. Technol.*, vol. 40, no. 15, pp. 2027–2036, 2019.
- [87] P. Das, S. Ghosh, and M. Baskey (Sen), "Heterogeneous catalytic reduction of 4-nitroaniline by rGO-Ni nanocomposite for water resource management," *J. Mater. Sci. Mater. Electron.*, vol. 30, no. 22, pp. 19731–19737, 2019.
- [88] K. Naseem, R. Begum, and Z. H. Farooqi, "Catalytic reduction of 2-nitroaniline: a review," *Environ. Sci. Pollut. Res.*, vol. 24, no. 7, pp. 6446–6460, 2017.
- [89] T. N. J. I. Edison, M. G. Sethuraman, and Y. R. Lee, "NaBH₄ reduction of ortho and para-nitroaniline catalyzed by silver nanoparticles synthesized using Tamarindus indica seed coat extract," *Res. Chem. Intermed.*, vol. 42, no. 2, pp. 713–724, 2016.
- [90] Y. Shiraishi and T. Hirai, "Selective organic transformations on titanium oxide-based photocatalysts," *J. Photochem. Photobiol. C Photochem. Rev.*, vol. 9, no. 4, pp. 157–170, 2008.
- [91] A. Alzamly *et al.*, "Tunable band gap of Bi³⁺-doped anatase TiO₂ for enhanced photocatalytic removal of acetaminophen under UV-visible light irradiation," *J. Water Reuse Desalin.*, vol. 9, no. 1, pp. 31–46, 2019.
- [92] J. Luan, Y. Shen, Y. Li, and Y. Paz, "The structural, photocatalytic property characterization and enhanced photocatalytic activities of novel photocatalysts Bi₂GaSbO₇ and Bi₂InSbO₇ during visible light irradiation," *Materials*, vol. 9, no. 10, pp. 801–819, 2016.
- [93] K. Imamura, S. Iwasaki, T. Maeda, K. Hashimoto, B. Ohtani, and H. Kominami, "Photocatalytic reduction of nitrobenzenes to aminobenzenes in aqueous suspensions of titanium(IV) oxide in the presence of hole scavengers under deaerated and aerated conditions," *Phys. Chem. Chem. Phys.*, vol. 13, no. 11, pp. 5114–5119, 2011.
- [94] W. Wu, R. Lin, L. Shen, R. Liang, R. Yuan, and L. Wu, "Visible-light-induced photocatalytic hydrogenation of 4-nitroaniline over In₂S₃ photocatalyst in water," *Catal. Commun.*, vol. 40, pp. 1–4, 2013.
- [95] W. Wu, S. Liang, Y. Chen, L. Shen, H. Zheng, and L. Wu, "High efficient photocatalytic reduction of 4-nitroaniline to p-phenylenediamine over microcrystalline SrBi₂Nb₂O₉," *Catal. Commun.*, vol. 17, pp. 39–42, 2012.
- [96] W. Wu *et al.*, "Efficient visible-light-induced photocatalytic reduction of 4-nitroaniline to p-phenylenediamine over nanocrystalline PbBi₂Nb₂O₉," *J. Catal.*, vol. 290, pp. 13–17, 2012.
- [97] J. Li, Y. Yu, and L. Zhang, "Bismuth oxyhalide nanomaterials: layered structures meet photocatalysis," *Nanoscale*, vol. 6, no. 15, pp. 8473–8488, 2014.

- [98] L. Ye, Y. Deng, L. Wang, H. Xie, and F. Su, "Bismuth-based photocatalysts for solar photocatalytic carbon dioxide conversion," *ChemSusChem*, vol. 12, no. 16, pp. 3671–3701, 2019.
- [99] P. Li *et al.*, "NaOH-induced formation of 3D flower-sphere BiOBr/Bi₄O₅Br₂ with proper-oxygen vacancies via in-situ self-template phase transformation method for antibiotic photodegradation," *Sci. Total Environ.*, vol. 715, pp. 136809–136823, 2020.
- [100] M. A. Gondal, C. Xiaofeng, and M. A. Dastageer, *Novel bismuth-oxyhalide-based materials and their applications*. Springer, 2017.
- [101] Y. Long *et al.*, "A novel solvent-free strategy for the synthesis of bismuth oxyhalides," *J. Mater. Chem. A*, vol. 6, no. 27, pp. 13005–13011, 2018.
- [102] Z. Ran *et al.*, "Bismuth and antimony-based oxyhalides and chalcogenides as potential optoelectronic materials," *npj Comput. Mater.*, vol. 4, no. 1, pp. 14–47, 2018.
- [103] H. Shi, M. A. Gondal, A. A. Al-Saadi, and X. Chang, "Visible-light-induced photodegradation enhancement of methyl orange over bismuth oxybromide through a semiconductor mediated process," *J. Adv. Oxid. Technol.*, vol. 18, no. 1, pp. 78–84, 2015.
- [104] S. Gao *et al.*, "Photocatalytic removal of tetrabromobisphenol A by magnetically separable flower-like BiOBr/BiOI/Fe₃O₄ hybrid nanocomposites under visible-light irradiation," *J. Hazard. Mater.*, vol. 331, pp. 1–12, 2017.
- [105] J. Di, J. Xia, H. Li, S. Guo, and S. Dai, "Bismuth oxyhalide layered materials for energy and environmental applications," *Nano Energy*, vol. 41, pp. 172–192, 2017.
- [106] R. Arthur, "Development of Bismuth Oxyhalide Photocatalysts for Environmental and Industrial Applications," Ph.D dissertation, College of Chem., Maine Univ., Orono, 2019.
- [107] H. Jia, W. He, B. Zhang, L. Yao, X. Yang, and Z. Zheng, "Facile synthesis of bismuth oxyhalide nanosheet films with distinct conduction type and photo-induced charge carrier behavior," *Appl. Surf. Sci.*, vol. 441, pp. 832–840, 2018.
- [108] G. Wang, X. Luo, Y. Huang, A. Kuang, Y. Hongkuan, and H. Chen, "BiOX/BiOY (X, Y = F, Cl, Br, I) superlattices for visible light photocatalytic applications," *RSC Adv.*, vol. 6, pp. 91508–91516, 2016.
- [109] F. A. Bannister, "The crystal-structure of the bismuth oxyhalides," *Mineral. Mag. J. Mineral. Soc.*, vol. 24, no. 149, pp. 49–58, 1935.
- [110] I. D. Sharma *et al.*, "One-pot synthesis of three bismuth oxyhalides (BiOCl, BiOBr, BiOI) and their photocatalytic properties in three different exposure conditions," *Cogent Chem.*, vol. 1, no. 1, pp. 1076371–1076386, 2015.

- [111] X. Zhang, Z. Ai, F. Jia, and L. Zhang, "Generalized one-pot synthesis, characterization, and photocatalytic activity of hierarchical BiOX (X = Cl, Br, I) nanoplate microspheres," *J. Phys. Chem. C*, vol. 112, no. 3, pp. 747–753, 2008.
- [112] H. AN, Y. DU, T. WANG, C. WANG, W. HAO, and J. ZHANG, "Photocatalytic properties of BiOX (X = Cl, Br, and I)," *Rare Met.*, vol. 27, no. 3, pp. 243–250, 2008.
- [113] Y. Lei, G. Wang, S. Song, W. Fan, and H. Zhang, "Synthesis, characterization and assembly of BiOCl nanostructure and their photocatalytic properties," *CrystEngComm*, vol. 11, no. 9, pp. 1857–1862, 2009.
- [114] B. Gao, A. Chakraborty, J.-M. Yang, and W. Lee, "Visible-light photocatalytic activity of BiOCl/Bi₃O₄Cl nanocomposites," *Bull. Korean Chem. Soc.*, vol. 31, pp. 1941–1944, 2010.
- [115] L. Kong, Z. Jiang, T. Xiao, L. Lu, M. O. Jones, and P. P. Edwards, "Exceptional visible-light-driven photocatalytic activity over BiOBr–ZnFe₂O₄ heterojunctions," *Chem. Commun.*, vol. 47, no. 19, pp. 5512–5514, 2011.
- [116] A. P. Chowdhury and B. H. Shambharkar, "Synthesis and characterization of BiOCl–Cu₂ZnSnS₄ heterostructure with enhanced photocatalytic activity," *Appl. Water Sci.*, vol. 8, no. 7, pp. 202–211, 2018.
- [117] C. Han, N. Zhang, and Y.-J. Xu, "Structural diversity of graphene materials and their multifarious roles in heterogeneous photocatalysis," *Nano Today*, vol. 11, no. 3, pp. 351–372, 2016.
- [118] S. Wang *et al.*, "Recent progress on visible light responsive heterojunctions for photocatalytic applications," *J. Mater. Sci. Technol.*, vol. 33, no. 1, pp. 1–22, 2017.
- [119] S. Juntrapirom, D. Tantraviwat, S. Suntalelat, O. Thongsook, S. Phanichphant, and B. Inceesungvorn, "Visible light photocatalytic performance and mechanism of highly efficient SnS/BiOI heterojunction," *J. Colloid Interface Sci.*, vol. 504, pp. 711–720, 2017.
- [120] S. Kumar, V. Sharma, K. Bhattacharyya, and V. Krishnan, "N-doped ZnO–MoS₂ binary heterojunctions: dual role of 2D MoS₂ in the enhancement of photostability and photocatalytic activity under visible light irradiation for tetracycline degradation," *Mater. Chem. Front.*, vol. 1, pp. 1093–1106, 2017.
- [121] D. Ma, H. Liu, J. Huang, J. Zhong, J. Li, and D. Wang, "Improved photocatalytic performance of flower-like BiOBr/BiOCl heterojunctions prepared by an ionic liquid assisted one-step hydrothermal method," *Mater. Lett.*, vol. 238, pp. 147–150, 2019.
- [122] C. Zhao *et al.*, "3D BiOBr/BiOCl heterostructure microspheres with enhanced photocatalytic activity," *J. Mater. Sci. Mater. Electron.*, vol. 31, no. 3, pp. 1868–1878, 2020.

- [123] J. Zhang, J. Lv, K. Dai, C. Liang, and Q. Liu, "One-step growth of nanosheet-assembled BiOCl/BiOBr microspheres for highly efficient visible photocatalytic performance," *Appl. Surf. Sci.*, vol. 430, pp. 639–646, 2018.
- [124] G. Liu, H. Xu, D. Li, Z. Zou, Q. Li, and D. Xia, "BiOCl/BiOBr heterojunction with rich oxygen vacancies induced by ultraviolet and its enhanced photocatalytic performance," *Eur. J. Inorg. Chem.*, vol. 2019, no. 46, pp. 4887–4893, 2019.
- [125] J. Tauc, "Absorption edge and internal electric fields in amorphous semiconductors," *Mater. Res. Bull.*, vol. 5, no. 8, pp. 721–729, 1970.
- [126] C.-C. Ting, S.-Y. Chen, and D.-M. Liu, "Structural evolution and optical properties of TiO₂ thin films prepared by thermal oxidation of sputtered Ti films," *J. Appl. Phys.*, vol. 88, pp. 4628–4633, 2000.
- [127] K.-Q. Lu, X. Xin, N. Zhang, Z.-R. Tang, and Y.-J. Xu, "Photoredox catalysis over graphene aerogel-supported composite," *J. Mater. Chem. A*, vol. 6, pp. 4590–4604, 2018.
- [128] C. Sriwong, K. Choojun, W. Tejangkura, and W. Prasanseang, "Preparation and photocatalytic activities of TiO₂-rGO nanocomposite catalysts for MB dye degradation over sunlight irradiation," *Mater. Sci. Forum*, vol. 936, pp. 47–52, 2018.
- [129] A. Samal, D. P. Das, K. K. Nanda, B. K. Mishra, J. Das, and A. Dash, "Reduced graphene oxide–Ag₃PO₄ heterostructure: a direct Z-scheme photocatalyst for augmented photoreactivity and stability," *Chem. Asian J.*, vol. 11, no. 4, pp. 584–595, 2016.
- [130] X. Hu, Q. Zhang, H. Nan, M. Wang, L. Qiao, and H. Tian, "Heterojunction Cu₂O/RGO/BiVO₄ ternary nanocomposites with enhanced photocatalytic activities towards degradation of rhodamine B and tetracycline hydrochloride," *New J. Chem.*, vol. 43, no. 46, pp. 18240–18250, 2019.
- [131] N. Zhang, M.-Q. Yang, S. Liu, Y. Sun, and Y.-J. Xu, "Waltzing with the versatile platform of graphene to synthesize composite photocatalysts," *Chem. Rev.*, vol. 115, no. 18, pp. 10307–10377, 2015.
- [132] S. Thakur and N. Karak, "Alternative methods and nature-based reagents for the reduction of graphene oxide: a review," *Carbon N. Y.*, vol. 94, pp. 224–242, 2015.
- [133] P. Cui, J. Lee, E. Hwang, and H. Lee, "One-pot reduction of graphene oxide at subzero temperatures," *Chem. Commun.*, vol. 47, no. 45, pp. 12370–12372, 2011.
- [134] S. Park and R. S. Ruoff, "Chemical methods for the production of graphenes," *Nat. Nanotechnol.*, vol. 4, no. 4, pp. 217–224, 2009.

- [135] J. Choi, N. D. K. Tu, S.-S. Lee, H. Lee, J. S. Kim, and H. Kim, "Controlled oxidation level of reduced graphene oxides and its effect on thermoelectric properties," *Macromol. Res.*, vol. 22, no. 10, pp. 1104–1108, 2014.
- [136] K. P. Loh, Q. Bao, G. Eda, and M. Chhowalla, "Graphene oxide as a chemically tunable platform for optical applications," *Nat. Chem.*, vol. 2, no. 12, pp. 1015–1024, 2010.
- [137] T. Wang *et al.*, "Reduced graphene oxide (rGO)/BiVO₄ composites with maximized interfacial coupling for visible light photocatalysis," *ACS Sustain. Chem. Eng.*, vol. 2, pp. 2253–2258, 2014.
- [138] M. Sohail *et al.*, "Synthesis of well-dispersed TiO₂@reduced graphene oxide (rGO) nanocomposites and their photocatalytic properties," *Mater. Res. Bull.*, vol. 90, pp. 125–130, 2017.
- [139] X. Li, W. Cai, L. Colombo, and R. S. Ruoff, "Evolution of graphene growth on Ni and Cu by carbon isotope labeling," *Nano Lett.*, vol. 9, no. 12, pp. 4268–4272, 2009.
- [140] F. Zhang, Y.-H. Li, J.-Y. Li, Z.-R. Tang, and Y.-J. Xu, "3D graphene-based gel photocatalysts for environmental pollutants degradation," *Environ. Pollut.*, vol. 253, pp. 365–376, 2019.
- [141] Y. Pan and D. Wu, "The rGO/BiOBr/Bi₄O₅Br₂ composites with stacked nanosheets for ciprofloxacin photodegradation under visible light irradiation," *Zeitschrift für Anorg. und Allg. Chemie*, vol. 645, no. 18–19, pp. 1153–1160, 2019.
- [142] K. Pramoda, U. Gupta, M. Chhetri, A. Bandyopadhyay, S. K. Pati, and C. N. R. Rao, "Nanocomposites of C₃N₄ with layers of MoS₂ and nitrogenated RGO, obtained by covalent cross-linking: synthesis, characterization, and HER Activity," *ACS Appl. Mater. Interfaces*, vol. 9, no. 12, pp. 10664–10672, 2017.
- [143] R. Zhang *et al.*, "Ternary Z-scheme heterojunction of Bi₂WO₆ with reduced graphene oxide (rGO) and Bi₂₅FeO₄₀ for enhanced visible-light photocatalysis," *J. Inorg. Organomet. Polym. Mater.*, vol. 30, pp. 2152–2162, 2020.

